

Detecting Atomic Shot Noise On Ultra-cold Atom Clouds

Gordon D. McDonald

A thesis submitted for the degree of
**Bachelor of Philosophy (Science) with Honours in Physics of
The Australian National University**

October, 2009

Declaration

This thesis is an account of research undertaken between February and October 2009 at The Department of Quantum Science, Research School of Physical Sciences and Engineering, The Australian National University, Canberra, Australia. Except where acknowledged in the customary manner, the material presented in this thesis is, to the best of my knowledge, original and has not been submitted in whole or part for a degree in any university.

Gordon D. McDonald
October, 2009

Acknowledgements

A great research group is formed by great people, and this is definitely a great group. Firstly, I would like to thank Nick Robins for his incredible puns, energy and willingness to help with whatever problem was at hand. Without your guidance, prodding, structure and help both in the lab and when writing up, this never would have been achieved. Thankyou to Daniel Döring for putting up with me in the lab, helping me to understand my data, always helping me to see where I could go next, proof reading (and offering to take the night shift on the machine ☺). Thanks to Cristina Figl for providing lots of encouragement and discussions, lots of code, and making my Matlab code work when everything was ~~packwurst~~. And thank you to Paul Altin for staying up late editing my drafts as the deadline approached. Thank you to my wonderful girlfriend Martina, for always being awesome (and helping out with the statistics that I didn't know). Of course I am indebted to my mother Debbie and my grandmother Pam for all the encouragement they gave me when things weren't working out. Emily, JD, Graham, Illiriana, Rachel, PJ, Mattias, Justin, Andrew, Joe, Michael and Emmanuel, you all made my time in at physics more enjoyable. Thankyou to all my honours cohort for making Honours fun. I would also like to thank the abundant and mysterious supplies of coffee and milk in the tearoom, and the ephemeral chocolate stash in the lab.

Abstract

Precise measurement of physical quantities underpins much of modern science and technology. Examples include length and time (satellite navigation), rotation and acceleration (guidance systems), electromagnetic (magnetic resonance imaging) and gravitational fields (mineral exploration). Currently, precision measurement of many physically and practically interesting quantities - such as the fine structure constant, the local gravitational field or any inertial acceleration - can be accomplished by atom interferometry [1]. Using *cold* atom interferometers may enable yet more precision, but this precision will be limited by atomic shot noise. Atomic shot noise, which is a fluctuation in the atomic density, arises because atoms are discrete. This fluctuation will affect precision when counting the atoms in a cloud, as is done in atomic interferometry. In this thesis, atomic shot noise was clearly and quantitatively measured in cold rubidium 87 atomic clouds using the absorption imaging technique. This was achieved by minimizing all possible sources of classical noise from the imaging setup, then binning the pixels together to overcome blurring effects. These blurring effects can be due to the velocity distribution of the atoms, the diffraction limit of the optical system, and the photon recoil in the measurement process itself. The tantalising possibility exists of measuring the shot noise on a Bose-Einstein condensate, and thereby gaining information on its quantum statistics. A scheme to produce and measure squeezing (a reduction in variance beyond the shot noise limit) in an atom laser beam will require a detector capable of measuring at the atomic shot noise limit, like the one developed in this thesis. At the moment, applying this technique to measuring the shot noise on a BEC is limited by the size of the condensate and the resolution of the imaging system, but in principle it should be possible, as this thesis demonstrates. A full calibration of the experimental setup is performed. The application of this work to increasing the precision of cold atom interferometry is discussed.

Contents

Declaration	iii
Acknowledgements	v
Abstract	vii
1 Introduction	3
2 Apparatus	7
2.1 Properties of ^{87}Rb	7
2.2 ^{87}Rb BEC Machine	9
3 The Theory Of Absorption Imaging	11
3.1 Imaging techniques	11
3.2 Measuring Atomic Density	12
3.2.1 Simple model	12
3.2.2 Complete model	12
3.3 Noise on Absorption Imaging	14
3.3.1 Atomic Noise	14
3.3.1.1 Ideal Boltzmann gas	14
3.3.1.2 Quantum Bose Gas	15
3.4 Laser Light Noise	16
3.4.1 Photon and electron statistics	16
3.4.2 Simple model	18
3.4.3 Complete model	19
3.4.4 Effect of classical fringes	20
3.5 Sources of blurring	21
3.5.1 Gravity	22
3.5.2 Temperature	23
3.5.3 Photon recoil in the imaging plane	23
3.5.4 Diffraction limit of optics	25
3.6 Old Images	25
4 The New System	27
4.1 Imaging setup	27
4.2 Camera Calibration	28
4.2.1 System gain	29
4.2.2 Quantum efficiency	31
4.2.3 Dark counts	32
4.3 Atom Cloud Calibration	32
4.3.1 Magnification of Imaging setup	33
4.3.2 Harmonic trap frequencies	33

4.3.3	Temperature calibration	34
4.3.3.1	Derivation of the Thermal Cloud Density	34
4.3.3.2	Calculation of the Optical Thickness of the Thermal Distribution	37
4.3.3.3	Derivation of the Density of the Condensate	38
4.3.3.4	Calculation of the Optical Thickness of the Condensate Fraction	41
4.3.3.5	Measurement of temperature	41
4.3.4	Number calibration	42
4.3.4.1	Derivation of condensate fraction	42
4.3.4.2	Measurement of condensate fraction	44
4.3.4.3	Calibration of atom number	45
4.4	What should it look like?	45
5	Observation of Atomic Shot Noise	49
6	Application to Atom Interferometry	53
6.1	Our Atom Interferometer	53
Conclusion and Outlook		57
A	Statistical Distributions	59
A.1	Poisson Distribution	59
A.1.1	General Properties	59
A.2	Approximations to mean and variance	60
A.3	Variance calculated by nearby averaging	61
Bibliography		65

Introduction

Physics is built on the interplay between theory and measurement. This is particularly true in the last decade and a half of progress in Bose-Einstein condensation, from the initial discovery of Bose-Einstein condensates (BEC) in dilute alkali gases [2] and the investigations into their basic properties [3, 4, 5], through to quantum correlation measurements [6, 7, 8, 9] and tests of the Bose-Hubbard model [10, 11] which describes bosons in an optical lattice.

But measurement itself is imprecise. Every measurement that is made has uncertainty, some of which stems from how much noise is present in the data. The impact of noise on a measurement can be quantified by its signal to noise ratio,

$$\frac{\text{Signal}}{\text{Noise}} \tag{1.1}$$

and this can be improved in two simple ways: by increasing the signal or reducing the noise. Understanding noise and subsequent reduction of noise is where this thesis will focus. Some noise sources can be eliminated¹. But some noise sources are inherent in the process and while they can be minimized, they cannot be completely removed. As an example consider a coherent laser beam. Quantum mechanics dictates that when counting the photons arriving from such a beam, there will always be fluctuations in the number that arrive in a certain time interval. These fluctuations, generally called photon shot noise, represent a fundamental limit to how well the intensity you measure will correspond to the time-averaged intensity of the beam. It is often possible to reduce the relative noise this imparts to a dataset by increasing the intensity of the laser beam², thereby improving the ratio (1.1), but it is not possible to completely remove such a noise source³.

The measurement tool analysed in this thesis is absorption imaging. It is the most common and one of the simplest imaging techniques for ultra-cold atom clouds. An image of the atoms is acquired by looking at the shadow cast upon a laser beam by a cloud of atoms. This is compared to an image with no atoms and the atomic density distribution is found. The question being asked in this thesis is: can we push the signal-to-noise ratio of the absorption image to the fundamental limits imposed by quantum mechanics? And if this is possible, can we detect a signal-to-noise ratio beyond the quantum limit⁴?

¹For example in this thesis, such noise sources are dust, unnecessary optical elements, and electronic noise from the equipment.

²However, any classical noise on your data will be amplified by this technique, and the best signal-to-noise ratio will be achieved at a compromise between these two effects.

³If the light can be persuaded to no longer be coherent, it is possible to reduce the fluctuations in photon counting. This is known as squeezing. However, this method introduces fluctuations in other variables which may be of interest.

⁴For example, can we detect a lower than classically expected fluctuation in the density of atoms in a

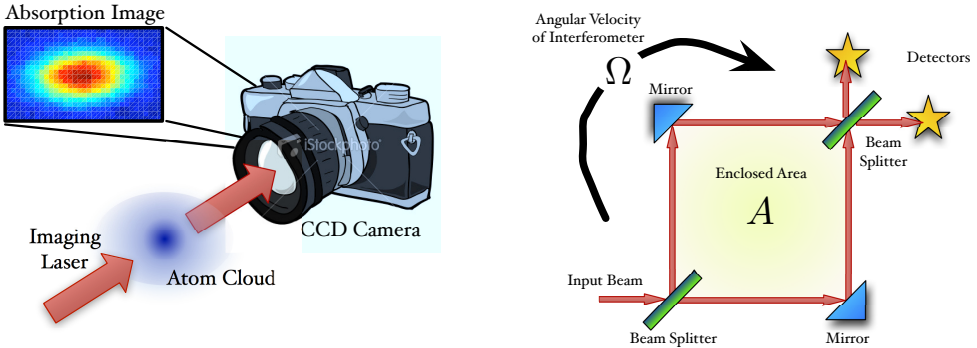


Figure 1.1: **Left:** Diagram illustrating absorption imaging, the measurement technique which this thesis will focus upon. **Right:** Schematic of a Sagnac interferometer, which can be used to measure rotation.

The quantum limit, otherwise referred to as shot noise, has been measured for decades and not always as an inconvenience. Another example where shot noise arises is in the precise measurement of current. Here, inherent fluctuations around the mean are also referred to as shot noise, and arise due to counting electrons instead of photons. In fact, the fractional quantum Hall effect, observed in the conduction properties of a 2D electron gas with a perpendicular magnetic field, can be directly observed by looking at the noise on current due to counting fractional charge quasi-particles, for examples see [12, 13]. Recently, the same experiment has been proposed in cold atom clouds trapped in an optical lattice [14]. Theoretically, fluctuations in atomic density on cold atom clouds have been investigated by many authors. The main difficulty is the absence of simple analytic solutions in the microcanonical ensemble⁵. Numerical solutions which apply to finite numbers of isolated atoms are of course possible (such as [15, 16, 17, 18, 6]). Experimentally, the absorption imaging technique has been used to measure quantum noise on a cold atom cloud in several notable instances. Fölling *et. al.* [7] used the technique to find the spatial noise correlation function of a cloud of ^{87}Rb atoms dropped from an optical lattice, thus revealing the periodicity of the lattice structure. Greiner *et. al.* [8] used the atom shot noise in absorption images to measure pair correlations (in space and momentum) in their cold fermionic cloud of ^{40}K atoms⁶. It should be noted, however, that they used a large amount of digital image processing (low and high pass filters) to reduce the classical fringes and camera noise on their image, in contrast to this thesis, where no image filtering is used to achieve atomic shot noise visibility. Esteve *et. al.* [19] measured the atomic density fluctuations in a quasi-1D ^{87}Rb Bose gas, again using absorption imaging. They

Bose-Einstein condensate?

⁵The microcanonical ensemble is a statistical mechanics concept which describes an isolated system which does not exchange particles or energy with a reservoir. This is the correct description of a cold atom cloud in a magnetic trap on short time scales, so that heating from current fluctuations in the trap and particle loss are not part of the description. This is in contrast to the canonical or grand-canonical ensembles which describe a system which is in equilibrium with a reservoir, due to exchanging either energy, or particles and energy, respectively. Most of the easy analytic solutions (especially the semiclassical ones presented in section 4.3) implicitly assume the grand-canonical ensemble, so it is a wonder they work at all, close to the condensation temperature T_c .

⁶They used a Feshbach resonance (a change in scattering length dependent upon the applied magnetic field) to create weakly attractive interactions to form molecules. These molecules were then dissociated by applying a radio-frequency field. The dissociated atoms are correlated because each pair moves apart in opposite directions with roughly equal speeds.

found qualitative agreement with the models of a 1D Bose gas (which has accurate analytic solutions), and the poissonian thermal statistics in the appropriate temperature regimes. However, their data is plagued by the same blurring as ours, with even more photon shot noise and consequently, their ‘agreement’ with theory is within a factor of 5. Their results do not directly apply to 3D BEC, since in a very elongated trap, the atoms at either end are not in contact (their separation is much larger than their de Broglie wavelength) and so they do not exhibit long-range coherence. Other methods of measuring atomic shot noise (and thus probing the quantum statistics of the atom cloud) have been used, such as in Chuu *et. al.*’s measurement of small BECs ($< 10^3$ atoms) of ^{87}Rb using fluorescence imaging [20]. They measured sub-poissonian (variance less than the number) atomic shot noise on Bose-condensed clouds with up to 500 atoms. This technique provides the required accuracy for small clouds, but absorption imaging provides a better signal-to-noise for clouds with roughly 10^3 atoms or more [20]. This thesis aims to see atomic shot noise without digital filtering such as used in [8], and with quantitative agreement as opposed to [19]. One long-term aim is to measure the quantum statistics of indistinguishable bosons using atomic shot noise. The other is being able to measure sub-poissonian atomic shot noise (squeezing) on larger clouds than [20], as squeezing techniques can be used to increase the sensitivity of cold-atom interferometry.

Squeezing is a general term for techniques that allow measurement with precision beyond the standard quantum limit [21]. That is, BECs could have atom density with variance less than poissonian [22]. Generally a squeezed state will allow more precise measurement of one variable, at the expense of the conjugate variable. For example, intensity or amplitude squeezing will allow more precise measurement of the atom number at one output port of an interferometer, at the expense of a greater uncertainty in the phase difference between the ports. Squeezing requires a nonlinear interaction term in the Hamiltonian, which can be from a nonlinear crystal (in the case of a laser) or from a two body interaction term in a BEC [22]. A BEC can also be squeezed by interaction with squeezed laser light [23].

In terms of the relative uncertainty in atom number $\frac{1}{\sqrt{N_{atoms}}}$, squeezing can be considered to change this factor to $\frac{\xi_N}{\sqrt{N_{atoms}}}$ where $\xi_N < 1$ is the number squeezing parameter. Estève *et. al.* [24] observed number squeezing in BECs using a one dimensional optical lattice in a magnetic trap, where the squeezing is obtained from the nonlinear inter-particle interactions. They achieved a best number squeezing⁷ of $\xi_N^2 = -6.6\text{dB}$ in a six-well lattice corresponding to $\xi_N = 0.5$.

Atomic interferometry has the advantage over light interferometry that atoms interact strongly with all of the fundamental forces, whereas light does so only weakly. This makes atoms a more attractive probe for measurement. Another advantage atoms have over light is inertial mass, the benefit of which is best illustrated by a small calculation. In interferometry, a measurement is made by comparing a reference signal (for example $\sin \omega t$) to a measurement signal (let’s say $\sin(\omega t + \phi)$). The phase difference ϕ can be related to the measurement quantity of interest. Interferometry can be used to measure rotation with

⁷However, as number squeezing is a trade off against phase coherence, a better measure of squeezing called the coherent squeezing parameter $\xi_S = \frac{\xi_N}{\langle \cos \phi \rangle}$ is used, where $\langle \cos \phi \rangle$ is a measure of phase coherence between the wells. The best coherent squeezing Estève *et. al.* achieved was $\xi_S^2 = -3.8\text{dB}$, also in a six-well lattice, corresponding to $\xi_N = 0.6$ and $\langle \cos \phi \rangle = 0.78$.

the setup depicted in Figure 1.1. Here the phase difference is given by the formula [1]

$$\phi = 8\pi c A \Omega E$$

where A is the area enclosed by the interferometer, Ω is the rotational velocity of the setup, E is energy of the particle used for measurement and c is the speed of light. In the case of atoms, E is the rest energy $E_{atom} = mc^2$ and in the case of photons, it is the energy per photon $E_{light} = hc/\lambda$. The precision achievable with the two techniques can be compared by taking the ratio of the phase differences, the larger the phase difference, the easier or more precise the measurement:

$$\begin{aligned} \frac{\phi_{atom}}{\phi_{light}} &= \frac{E_{atom}}{E_{light}} \\ &= \frac{m_{atom} c \lambda_{light}}{h} \\ &\approx \frac{10^{-25} \times (3 \times 10^8) \times 10^{-7}}{7 \times 10^{-34}} \\ &\approx 10^{10}. \end{aligned} \quad (1.2)$$

Theoretically, ten orders of magnitude more precision appears to be achievable with atomic interferometers⁸! But there is yet another possibility. Just as temporally coherent light from laser beams improved the precision available from light interferometry, so too may coherent atom sources improve the precision of atom interferometry, by the ability to squeeze the atom source. Hot and cold atom interferometers are already in use [1, 25, 26, 27] for a multitude of precise measurements. The fine structure constant α , which sets the strength of electromagnetic interactions, has been measured using atom interferometry to a relative accuracy of 7×10^{-9} [28, 29], which is roughly half as accurate as the best measurement of α using the quantum Hall effect. There are plans underway to gain an order of magnitude in precision [30] using atomic interferometry. Cold atom interferometers are also used to measure the local gravitational field very precisely [31] which has applications in navigation and mineral exploration, and has been proposed for tests of general relativity [32] in which the interferometer would be a gravitational wave detector with comparable sensitivity to the best light-based interferometers.

Whether or not the precision of cold atom interferometers will eventually live up to the bold promise of (1.2) is a difficult question to answer theoretically. To answer the question by experiment, our detection tool - absorption imaging - must be able to image at the atomic shot-noise limit. Only then we can detect if we are able to squeeze the atom interferometer, and thereby increase our measurement precision. So this is the quest we embark upon; analytically and quantitatively reducing the noise on absorption images of cold-atom clouds, searching for the quantum limit of atomic shot-noise.

⁸At present their advantages are not fully realised though, because a laser can produce many more photons per second than an atom laser can produce atoms per second. This, however, is merely an engineering challenge.

Apparatus

In this chapter, we briefly describe the apparatus used to prepare samples of ultra-cold ^{87}Rb to study atomic shot noise.

2.1 Properties of ^{87}Rb

There are two naturally occurring isotopes of rubidium, ^{85}Rb (72%) and ^{87}Rb (28%). They have several electronic transitions at 780nm, well within the capabilities of cheap and readily available diode lasers¹. An important step in the standard technique for achieving BEC in dilute alkali gases is the evaporative cooling stage, in which the most energetic atoms are allowed to leave the system, and the remainder rethermalise at a lower temperature. This rethermalisation relies heavily upon the collisional scattering cross-section of the species of interest. The collisional properties of ^{87}Rb make it particularly well-suited to evaporation [34, 35], making the condensation of ^{87}Rb relatively straightforward. Some of the relevant physical properties of ^{87}Rb are listed in the table below.

Property	Value	Source
Mass	$86.91 \text{ g/mol} = 1.4432 \times 10^{-25} \text{ kg}$	[36]
Natural Abundance	27.83(2) %	[36]
Atomic Number	37	[37]
Ground State Electronic Configuration	[Kr] 5s ¹	[36]
Particle Type	Composite Boson	[37]
Nuclear Spin I	3/2	[38]
S -wave Scattering Length a	5.77 nm	[39]
Thermal de Broglie Wavelength λ_T	$\lambda_T^2 T = 35.07 \mu\text{m}^2 \text{nK}$	$\lambda_T = \frac{\hbar}{\sqrt{2\pi m k_B T}}$
$5^2\text{S}_{1/2} \rightarrow 5^2\text{P}_{3/2}$ Optical Transition		
Wavelength λ	780.24 nm (<i>Vacuum</i>)	[38]
Natural Linewidth Γ	$2\pi \times 6.066 \text{ MHz}$	[38]
$ F=2, m_F=\pm 2\rangle \rightarrow F'=3, m'_F=\pm 3\rangle$	σ^\pm closed cycling transition	
Resonant cross-sectional area σ_0	$2.906 \times 10^{-9} \text{ cm}^2$	[38]
Saturation intensity I_{sat}	1.669 mW/cm ²	[38]

Table 2.1: Some properties of ^{87}Rb .

¹A 10mW laser diode will set you back around \$25 [33].

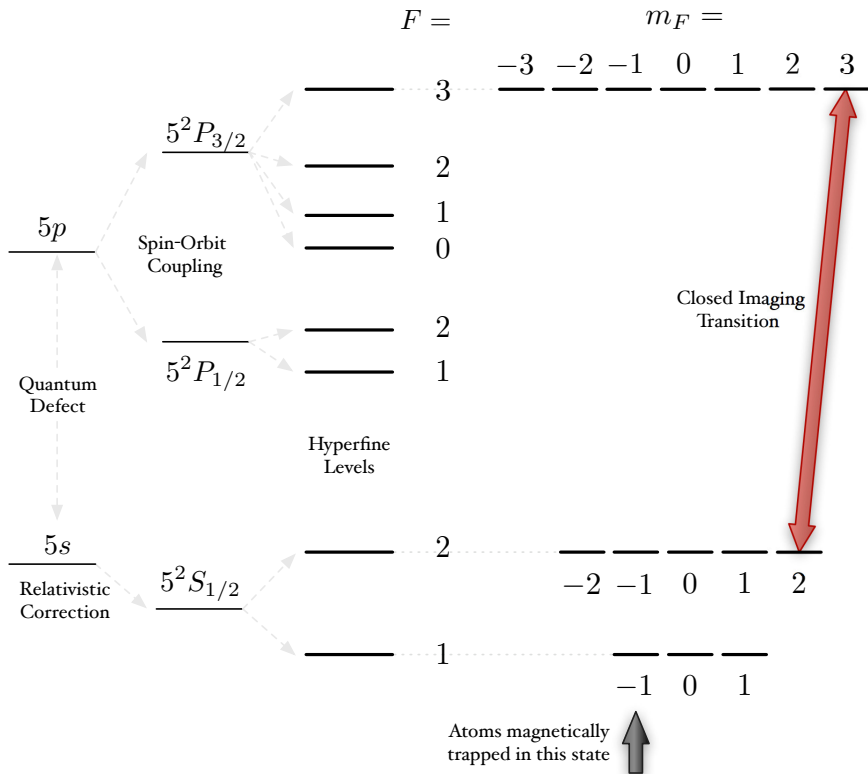
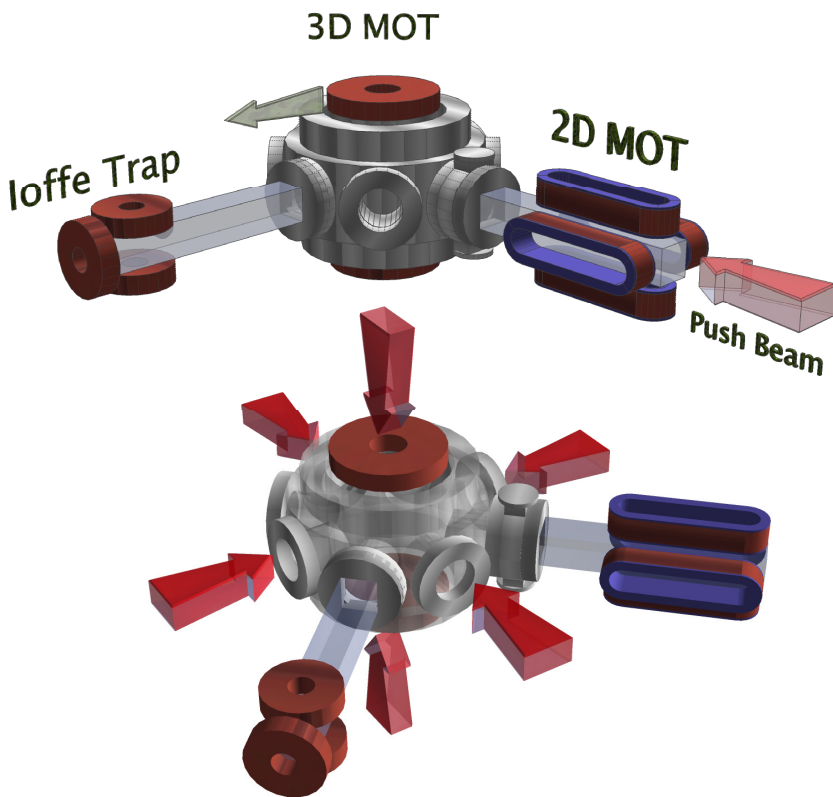


Figure 2.1: **Above:** Hyperfine level splitting of ^{87}Rb . **Below, Top:** Diagram of the key parts of the ^{87}Rb BEC machine. The arrow next to the 3D MOT shows the direction in which its quadrupole coils move (on a robotic stage, not shown) to transfer the atoms into the Ioffe coils for evaporative cooling. **Below, Bottom:** The 3 pairs of orthogonal laser beams which, together with the two coils, make up the 3D Magneto-Optical Trap.



2.2 ^{87}Rb BEC Machine

To make a ^{87}Rb BEC, our setup requires several stages of collection and cooling. It all begins in the 2D Magneto-optical trap (MOT). In the 2D MOT glass cell, the rubidium vapor is kept at the saturation pressure, which is roughly 10^{-7} Torr for the laboratory temperature of 16°C . Elongated quadrupole magnetic fields are applied as per Figure 2.1, to confine the atoms to a narrow line down the centre of the first glass cell. A laser ‘push beam’ (locked on the $|F = 2, m_F\rangle$ to $|F' = 3, m_{F'}\rangle$ transition²) directs the atoms through a tiny opening into a different vacuum chamber (at about 10^{-11} Torr ambient pressure) in which the atoms are collected and cooled in a 3D MOT.

The 3D Magneto-optical trap consists of a quadrupole magnetic field with six circularly polarised laser beams in three orthogonal directions which are slightly detuned below the resonant frequency. It works by confining the atoms in both position (via the Zeeman shift in the optical resonance as the atoms move off-centre in the magnetic field) and velocity space (via the Doppler shift in the optical resonance as the velocity increases toward the source of the beam). The force experienced by the atoms can be approximately expressed as [37]

$$\mathbf{F}_{\text{3DMOT}} \approx -2 \frac{\partial F}{\partial \omega} (k\mathbf{v} + \beta\mathbf{r})$$

where the velocity of the atom is \mathbf{v} , the atom’s displacement from the centre of the trap \mathbf{r} , the wave number and frequency of the laser light are k and ω , β is the Zeeman shift given component-wise by

$$\beta\mathbf{r}_i = \frac{gJ\mu_B}{\hbar} \frac{\partial B}{\partial x_i} \mathbf{r}_i$$

and

$$\frac{\partial F}{\partial \omega} = \frac{\hbar\Gamma I}{2cI_{\text{sat}}} \frac{\partial}{\partial \omega} \frac{\omega}{1 + \frac{I}{I_{\text{sat}}} + \left(\frac{2[\omega - \omega_0]}{\Gamma}\right)^2},$$

and the resonant frequency of the atomic transition is given by ω_0 .

We have about 10^{10} atoms at this point, as measured by fluorescence in the MOT. Polarisation gradient cooling³ is applied for a few milliseconds, followed by optical pumping into the $|1, -1\rangle$ ground state. Approximately 50% of the atoms make it into the $|1, -1\rangle$ state as the optical pumping is turned off, as some end up in the untrapped $|1, 0\rangle$ state and some land in the $|1, 1\rangle$ state which is repelled from the centre of the trap. A robotic stage then transfers the atoms in the 3D MOT quadrupole coils to the Ioffe-Pritchard magnetic trap. The transfer between the magnetic traps is affected by how well they are ‘mode-matched’, which includes the geometry of the potential seen by the atoms, and the speed with which the transfer takes place. Now there are around 10^8 atoms in the Ioffe trap. Here, we begin radio frequency (RF) evaporative cooling from around 60 MHz to a final frequency of between 5 and 1 MHz depending upon the size of the cloud and the

²Throughout this section, the notation $|F, m_F\rangle$ is used to represent the internal state of the atoms. F is the total angular momentum, and m_F is the component of the angular momentum in the direction \hat{B} where \vec{B} is the magnetic field at the location of the atoms.

³Polarisation gradient cooling allows laser cooling to achieve dramatically sub-Doppler temperatures by showing the atoms a gradient in the potential energy due to a periodically changing light polarisation in a standing wave. The atoms are more likely to emit a photon at the top of the gradient, and this puts them at the bottom again. In this way they are always travelling ‘uphill’ so they lose energy. See, for example, [37].

temperature required⁴. During this stage it is important to confine the atoms enough to allow two-body collisions and rethermalization, to make the evaporative cooling efficient. At the completion of a suitably low RF evaporation sequence (down to about 1 MHz) we have an atom cloud with a sizable BEC.

Having produced a BEC, there are various options for what we may do with the cloud. The stock-standard ‘ballistic expansion’ is simply to turn off the confining magnetic field and allow the atoms to fall under gravity, expanding as they fall due to their momentum width.

Another option is to use an RF pulse to transfer a fraction of the $|1, -1\rangle$ atoms into the $|1, 0\rangle$ state so that they are no longer held by the confining magnetic field and will thus fall under gravity while the majority of the atoms are still trapped. This is known as radio frequency outcoupling, as the radio frequency field couples the trapped $|1, -1\rangle$ state and the untrapped $|1, 0\rangle$ state. Leaving the pulse on for a slightly longer duration can create a continuous⁵ outcoupling (see Figure 3.4), while increasing the amplitude of the coupling and the duration can allow for coupling to the ‘anti-trapped’ $|1, 1\rangle$ state in which the atoms are repelled from the centre of the magnetic trap, as well as being pulled down by gravity.

After we have an out-coupled pulse, we can do interesting things with it. For example, to create an interferometer we split the out-coupled pulse into separate m_F states soon after it is generated, then recombine the pulses later and count how many atoms are in each final m_F state (see Chapter 6).

Imaging takes place after the atoms are repumped from the $|1, -1\rangle$ state into the $|2, 2\rangle$ state. The $|2, 2\rangle \rightarrow |3, 3\rangle$ transition is used as it is a closed transition, because the excited state $|3, 3\rangle$ can only decay into the $|2, 2\rangle$ state. Thus, each atom can be treated simply as a two level system. Imaging will be treated in detail in Chapter 3.

⁴The radio-frequency field is applied by a small one-loop coil next to the glass cell in which the atoms are. For an overview of evaporative cooling in BECs, see [35].

⁵Continuous for a small amount of time, eventually the BEC will run out of atoms.

The Theory Of Absorption Imaging

Having produced the cold atom sample, we now proceed to analyse the measurement of the atom cloud. This chapter presents a rigorous theoretical description of the technique of absorption imaging. We first discuss alternative imaging techniques, and the reason for the choice of absorption imaging.

3.1 Imaging techniques

Absorption imaging involves a minimum of two images. The first, $I_f(x, y)$, is a picture of the intensity profile of the imaging laser beam, with the shadow of the atoms cast upon it. The second picture, $I_0(x, y)$, is taken after the atoms have fallen out of the camera's view, so that the profile of the imaging laser beam can be recorded by itself. It achieves high signal to noise in large atom clouds, but it saturates at high density¹, and its measurement precision is affected by lensing² for small detunings from the atomic resonance and high densities. Absorption imaging has the disadvantage of a high heating rate due to photon recoil (see section 3.5.3), making it a destructive imaging technique.

Dispersive imaging methods require the use of scattered light. These include dark-ground imaging, and phase contrast imaging. In dark-ground imaging, a screen in the Fourier plane blocks the unscattered light, so the signal comes from the scattered light alone. For low atom densities this technique has a signal which is quadratic in atomic density, making it insensitive to small atom clouds[40]. Phase contrast imaging uses the unscattered light as the local oscillator for a sort of homodyne detection [40]. The scattered light is phase shifted by $\pi/2$ in the Fourier plane, so that it interferes with the scattered light. Phase contrast imaging has the advantage that at low atom densities its signal is linear in density, however, it is still a factor of 2 behind absorption imaging [40]. Dispersive imaging techniques have two advantages. The first is that the measurement signal is cyclic (as a phase is measured) so that they do not saturate at high atom number. The second advantage is that for the same amount of heating (due to photon recoil), dispersive imaging techniques obtain more signal than absorption imaging. They can be made relatively non-destructive, and this allows repeated measurements on a single atom cloud.

Fluorescence imaging provides a lower signal than the other techniques, but it has the advantage of lower background noise [40]. Its signal-to-noise makes it the optimum technique for detecting atom clouds with less than 10^3 atoms [20]. However with larger atom clouds, its signal becomes typically 100 times lower than that from absorption imaging.

¹This can be alleviated by detuning from the atomic resonance.

²The index of refraction of the cloud is proportional to atomic density. For our analysis of imaging, we assume that this lensing effect is minimal.

As our atom clouds are typically on the order of 10^5 to 10^6 atoms, are not prohibitively dense after ballistic expansion, and as we do not require multiple measurements of the same cloud, absorption imaging has been chosen as our measurement technique.

3.2 Measuring Atomic Density

3.2.1 Simple model

We begin the analysis of absorption imaging by assuming the atoms are acting as independent two-level systems. Let the atoms have a volume density $\rho(x, y, z)$. Those atoms in the path of the laser reduce the light's intensity I according to Beer's law;

$$\frac{dI}{dz} = -\rho\sigma I \quad (3.1)$$

where σ is the optical cross section of the atoms[37],

$$\sigma = \frac{\sigma_0}{\left(\frac{2\Delta}{\Gamma}\right)^2 + 1} \quad (3.2)$$

which is a function of the detuning from atomic resonance $\Delta = \omega - \omega_0$, the linewidth of the transition Γ and the resonant cross-sectional area $\sigma_0 = \frac{3\lambda_0^2}{2\pi}$. So from (3.1)

$$\begin{aligned} \int_{I_0}^{I_f} \frac{1}{I} dI &= \int_{-\infty}^{\infty} -\rho\sigma dz \\ I_f &= I_0 e^{-n\sigma} \end{aligned} \quad (3.3)$$

where $n(x, y) = \int_{-\infty}^{\infty} \rho(x, y, z) dz$ is now the column density of atoms per unit area in the xy plane. Thus if we can measure I_0 and I_f , we can calculate $n(x, y)$ as follows

$$n(x, y) = \frac{1}{\sigma} \ln \left(\frac{I_0(x, y)}{I_f(x, y)} \right). \quad (3.4)$$

In the actual experiment we will not be measuring continuous functions, but rather pixelated samples of those continuous functions. This will introduce some approximation into our measurement as

$$\underbrace{\ln \left(\frac{1}{A} \int_A I(x, y) dx dy \right)}_{\text{what we will calculate}} \neq \underbrace{\frac{1}{A} \int_A \ln I(x, y) dx dy}_{\text{the correct expression}} \quad (3.5)$$

where A is the area occupied by one pixel. The approximation will improve with smaller pixels or flatter intensity distributions, until the area of the pixel is small enough that the intensity is constant over an entire pixel, at which point the approximation becomes exact.

3.2.2 Complete model

Next, we maintain the assumption that our atoms act as independent two-level systems, but we include two extra facts:

1. The atoms can be saturated, so that at high intensity the relationship $\frac{dI}{dz} \propto I$ no longer holds. In fact the correct way to include this in the semi-classical model is to

adjust σ so that

$$\sigma_c = \frac{\sigma_0}{\left(\frac{2\Delta}{\Gamma}\right)^2 + 1 + \frac{I}{I_{sat}}} \quad (3.6)$$

where $I_{sat} = \frac{\pi hc\Gamma}{3\lambda_0^3}$ is the on-resonance saturation intensity.

2. Not all the light can be absorbed by the correct transition³, so as a general correction we may say that a fraction α is absorbable, i.e.

$$\frac{dI_a}{dz} = -\rho\sigma_c I_a \quad (3.7)$$

where $I_{a0} = \alpha I_0$.

Given the corrections (3.6) and (3.7), we see that

$$\frac{dI_a}{dz} = \frac{-\rho\sigma_0 I_a}{\left(\frac{2\Delta}{\Gamma}\right)^2 + 1 + \frac{I_a}{I_{sat}}} \quad (3.7)$$

so that

$$\begin{aligned} \int_{I_{a0}}^{I_{af}} \left(\frac{\left(\frac{2\Delta}{\Gamma}\right)^2 + 1}{I_a} + \frac{1}{I_{sat}} \right) dI_a &= - \int_{-\infty}^{\infty} \rho(x, y, z) \sigma_0 dz \\ \left[\left(\frac{2\Delta}{\Gamma}\right)^2 + 1 \right] \ln \frac{I_{af}}{I_{a0}} + \frac{I_{af} - I_{a0}}{I_{sat}} &= -n(x, y) \sigma_0 \end{aligned}$$

and relabeling $L = \left(\frac{2\Delta}{\Gamma}\right)^2 + 1$, we have

$$n(x, y) = \frac{1}{\sigma_0} \left[\frac{I_{a0f} - I_{af}}{I_{sat}} + L \ln \frac{I_{a0}}{I_{af}} \right], \quad (3.8)$$

which would appear to be the end of the problem.

However, what we will measure on the camera is $I_0 = I_{a0}/\alpha$ and $I_f = I_{af} + (1 - \alpha) I_0$, as the camera cannot distinguish between light which the atoms can and cannot absorb. Thus we have

$$\begin{aligned} n(x, y) &= \frac{1}{\sigma_0} \left[\frac{\alpha I_0 - I_f + (1 - \alpha) I_0}{I_{sat}} + L \ln \left(\frac{\alpha I_0}{I_f + (\alpha - 1) I_0} \right) \right] \\ n(x, y) &= \frac{1}{\sigma_0} \left[\frac{I_0 - I_f}{I_{sat}} + L \ln \left(\frac{\alpha I_0}{I_f + (\alpha - 1) I_0} \right) \right]. \end{aligned} \quad (3.9)$$

This is the equation which will be applied to calculate the atom column density $n(x, y)$ on a pixel by pixel basis. Note that this expression is also subject to the problem described in inequality (3.5), and that in the case where $\alpha = 1$ and $I_{sat} \rightarrow \infty$ equation (3.9) reduces to equation (3.4).

Figure 3.1 demonstrates the impact that *not* including these corrections will have on imaging. Optical depth here refers to the quantity $\ln \frac{I_0}{I_f}$.

³Due to imperfect polarization, etc.

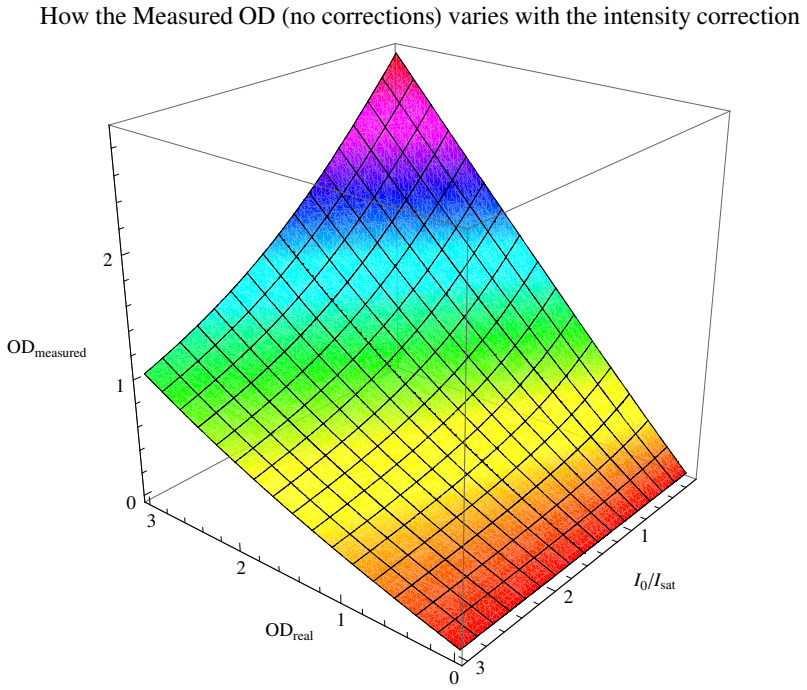


Figure 3.1: How the measured OD ($= \ln \frac{I_0}{I_f}$) varies, with and without the intensity correction term in equation (3.9). The effect is shown in this graph, for on-resonance light ($\Delta = 0, L = 1$). The measured OD will be much lower than the real OD at high intensities or a high detuning, in these instances a lower atom density will be measured as well. It is not always feasible or desirable to operate in a low-intensity regime, so the intensity correction term is required.

3.3 Noise on Absorption Imaging

3.3.1 Atomic Noise

3.3.1.1 Ideal Boltzmann gas

In an ideal Boltzmann gas it is possible to derive the fluctuation around the mean number of particles $\langle n \rangle = \rho v$ in a given volume v , where the total number of particles in the gas is $N = \rho V$ and the total volume of the gas is V . This can be done [41] by considering the probability that in a gas consisting of one particle, the particle is instantaneously in the volume $v \leq V$. Assuming ergodicity, this is given by the ratio v/V . The probability that there are n particles in this volume, given that the gas contains a total of N particles is given by the binomial distribution;

$$P(n \text{ particles in a volume } v) = \binom{N}{n} \left[\frac{v}{V} \right]^n \left[1 - \frac{v}{V} \right]^{n-N}. \quad (3.10)$$

Since this probability is binomial, if we take the thermodynamic limit that $N \rightarrow \infty$ and the limit that $v \ll V$ so that $v/V \rightarrow 0$, noting of course that

$$\begin{aligned} N \frac{v}{V} &= \rho v \\ &= \langle n \rangle \end{aligned}$$

which may be held constant throughout the limit, we arrive at a Poisson distribution (see section A.1)

$$P(n \ll N \text{ particles in a volume } v \ll V) = \frac{\langle n \rangle^n e^{\langle n \rangle}}{n!} \quad (3.11)$$

which gives the variance of the particle number about its mean value as

$$\text{Var}(n) = \langle n \rangle.$$

So, in an ideal Boltzmann gas, the variance in the number of particles in a given small volume is equal to the mean number in that volume.

3.3.1.2 Quantum Bose Gas

The equations (3.10) and (3.11) also hold for non-interacting bosons in a box⁴ [42]. In general the variation in number density is given in this case from the second order correlation function which is defined by [43]

$$\begin{aligned} g_2(\mathbf{r}_1, \mathbf{r}_2) &= \frac{\langle \hat{\psi}^\dagger(\mathbf{r}_1)\hat{\psi}^\dagger(\mathbf{r}_2)\hat{\psi}(\mathbf{r}_1)\hat{\psi}(\mathbf{r}_2) \rangle}{\langle \hat{\psi}^\dagger(\mathbf{r}_1)\hat{\psi}(\mathbf{r}_1) \rangle \langle \hat{\psi}^\dagger(\mathbf{r}_2)\hat{\psi}(\mathbf{r}_2) \rangle} \\ &= \frac{\langle \hat{\psi}^\dagger(\mathbf{r}_1)\hat{\psi}^\dagger(\mathbf{r}_2)\hat{\psi}(\mathbf{r}_1)\hat{\psi}(\mathbf{r}_2) \rangle}{\langle \hat{\rho}(\mathbf{r}_1) \rangle \langle \hat{\rho}(\mathbf{r}_2) \rangle}. \end{aligned}$$

where $\hat{\psi}(\mathbf{r}, t)$ is the bosonic annihilation operator at the position \mathbf{r} , and can be written in terms of the energy eigenstate annihilation operators \hat{a}_i

$$\hat{\psi}(\mathbf{r}, t) = \delta(\mathbf{r} - \mathbf{r}', t - t') \sum_i c_i \hat{a}_i.$$

If we now define for small \mathbf{r}

$$g_2(\mathbf{r}) = g_2(\mathbf{R}, \mathbf{R} - \mathbf{r})$$

and then take $\mathbf{r} \rightarrow 0$ we see that

$$\begin{aligned} g_2(0) &= \frac{\langle \hat{\psi}^\dagger(\mathbf{R})\hat{\psi}^\dagger(\mathbf{R})\hat{\psi}(\mathbf{R})\hat{\psi}(\mathbf{R}) \rangle}{\langle \hat{\rho}(\mathbf{R}) \rangle^2} \\ &= \frac{\langle \hat{\rho}(\mathbf{R})^2 \rangle}{\langle \hat{\rho}(\mathbf{R}) \rangle^2}, \end{aligned}$$

and the variance in number density (at a point) is given by

$$\begin{aligned} \text{Var}(\rho) &= \langle \hat{\rho}(\mathbf{R})^2 \rangle - \langle \hat{\rho}(\mathbf{R}) \rangle^2 \\ &= [g_2(0) - 1] \langle \hat{\rho} \rangle^2. \end{aligned} \quad (3.12)$$

⁴Although, in [42] the distributions are derived in the form of cumulant generating functions rather than probability distribution. However, the two forms are equivalent.

The generalization to a larger volume is given by [41]

$$\text{Var}(n) = \left[\int g_2(\mathbf{r}) dV - 1 \right] \langle n \rangle^2 \quad (3.13)$$

where $n = \int \rho dV$ is the number of particles in the volume. According to [40], $g_2(0) = 2$ for a thermal cloud and $g_2(0) = 1$ for a BEC.

3.4 Laser Light Noise

3.4.1 Photon and electron statistics

An important point to note is that, in a given image, the statistics of the count at a pixel arises directly from the electron statistics and only indirectly from the statistics of the laser light. If we have a Poisson-distributed random number of photons N arriving at a detector in a time t , then the probability that exactly n photons hit the detector in time t is given by

$$Pr(N = n) = \frac{(kt)^n e^{-kt}}{n!} \quad (3.14)$$

where k is the constant average rate at which photons hit the detector over a long time period,

$$\begin{aligned} k &\equiv \left\langle \frac{dn}{dt} \right\rangle \\ &= \frac{IA_{\text{pixel}}}{E_{\text{photon}}} \end{aligned}$$

and is equal to the intensity of the light I times the area of the detector (pixel) A_{pixel} divided by the energy of one photon E_{photon} . Now assume that the detector detects some of the photons that hit it, some not. Say the probability of a detection, given that there is a hit, is p . Thus, given there were n total hits, the probability that the number detected M , equals some number m , is binomial;

$$Pr(M = m | N = n) = \binom{n}{m} p^m (1-p)^{n-m}.$$

We can combine these two to find the probability of m photons being detected at the detector in a time t . Since

$$Pr(M = m) = \sum_{\text{all possible } n} Pr(M = m | N = n) Pr(N = n)$$

by conditional probability, we have

$$\begin{aligned}
Pr(M = m) &= \sum_{i=0}^{\infty} Pr(M = m | N = m + i) Pr(N = m + i) \\
&= \sum_{i=0}^{\infty} \binom{m+i}{m} p^m (1-p)^i \frac{(kt)^{m+i} e^{-kt}}{(m+i)!} \\
&= \sum_{i=0}^{\infty} \frac{(m+i)!}{m! i!} p^m (1-p)^i \frac{(kt)^{m+i} e^{-kt}}{(m+i)!} \\
&= \left(\sum_{i=0}^{\infty} \frac{[kt(1-p)]^i e^{-kt(1-p)}}{i!} \right) \frac{(pkt)^m e^{-ktp}}{m!}.
\end{aligned}$$

Now the term in brackets is the sum over all probability of a Poisson distribution with mean $kt(1-p)$, so it is exactly 1. Thus

$$Pr(M = m) = \frac{(pkt)^m e^{-ktp}}{m!}$$

which is a Poisson distribution with mean and variance ktp .

So a CCD pixel with a quantum efficiency p and covering an area A , taking a picture of a light source with poissonian statistics 3.14, intensity I and energy per photon of E , and using an exposure time of t , has a probability of acquiring m electrons in its well of

$$\begin{aligned}
Pr(M = m) &= \frac{(pkt)^m e^{-ktp}}{m!} \\
&= \frac{\left(\frac{pIAt}{E}\right)^m e^{-\frac{pIAt}{E}}}{m!}
\end{aligned} \tag{3.15}$$

which is Poissonian with mean and variance

$$\langle m \rangle = \frac{pIAt}{E}. \tag{3.16}$$

Now when the camera takes an image, the number of electrons m in each well are counted. The number of electrons is then effectively multiplied⁵ by a number s called the *System Gain*, to arrive at the number of counts ϕ for that pixel;

$$\phi = sm \tag{3.17}$$

and thus to calculate the ‘intensity’ I_m on a pixel we use

$$\begin{aligned}
m &= \frac{\phi}{s} \\
pI_n At/E &= \frac{\phi}{s} \\
I_n &= \frac{\phi E}{spAt}
\end{aligned}$$

⁵During the analog to digital conversion (ADC). Note that s also includes any post-ADC multiplication factor, such as a software multiplication.

But to calculate the variance we will measure in the intensity, $\text{Var}(I_n)$, we use (from equations (3.14),(3.15))

$$\begin{aligned}\text{Var}(m) &= p\text{Var}(n) \\ \langle m \rangle &= p\text{Var}\left(\frac{I_n At}{E}\right) \\ p\langle I \rangle At/E &= \frac{pA^2 t^2}{E^2} \text{Var}(I_n) \\ \text{Var}(I_n) &= \frac{E}{At} \langle I_n \rangle.\end{aligned}$$

In the subsequent sections it is easier to work with electron count m instead of intensity I . The conversion is supplied by equation (3.16), which can also be used to convert I_{sat} in equation (3.9) into $m_{sat} = pI_{sat}At/E$. Thus the expression (3.9) for the column density of atoms per unit area becomes

$$n(x, y) = \frac{1}{\sigma_0} \left[\frac{m_0 - m_f}{m_{sat}} + L \ln \left(\frac{\alpha m_0}{m_f + (\alpha - 1)m_0} \right) \right]. \quad (3.18)$$

This is the actual equation implemented to calculate the atom density from the images.

3.4.2 Simple model

As described in the previous section, the electron count m_0 with no atoms will have poissonian statistics⁶, i.e.

$$\text{E}(m_0) = \text{Var}(m_0) = \hat{m}_0.$$

The light which has passed through the atoms is still coherent⁷, but with lower intensity. It will thus also have poissonian statistics

$$\text{E}(I_f) = \text{Var}(I_f) = \hat{I}_f = \hat{I}_0 e^{-\hat{n}\sigma}.$$

from equation (3.3). Thus the electron count will also be exponentially reduced, but still poissonian (following the discussion in the previous section):

$$\begin{aligned}\text{E}(m_f) &= \text{Var}(m_f) = \hat{m}_f. \\ &= \hat{m}_0 e^{-\hat{n}\sigma}.\end{aligned}$$

⁶Commonly referred to as photon shot noise.

⁷CCD cameras are phase insensitive, so we need not worry here about the phase difference [40] the light acquires when travelling through the atom cloud.

Now we are interested in the variance which this introduces into our calculation of $n(x, y)$ from equation (3.4),

$$\begin{aligned} n(x, y) &= \frac{1}{\sigma} \ln \left(\frac{I_0(x, y)}{I_f(x, y)} \right) \\ &= \frac{1}{\sigma} \ln \left(\frac{m_0(x, y)}{m_f(x, y)} \right) \\ &= \frac{1}{\sigma} (\ln m_0 - \ln m_f) \end{aligned}$$

Note that σ here refers to the optical cross-section of the imaging transition, not a standard deviation. This variance may be calculated by propagation of errors, or by applying the approximate mean and variance formulas discussed in section A.2. Here we will use propagation of errors, so we have

$$\begin{aligned} (dn)_{photon}^2 &= \frac{1}{\sigma^2} \left[\left(dm_0 \cdot \frac{\partial}{\partial \hat{m}_0} \ln \hat{m}_0 \right)^2 + \left(dm_f \cdot \frac{\partial}{\partial \hat{m}_f} \ln \hat{m}_f \right)^2 \right] \\ &= \frac{1}{\sigma^2} \left[\left(\frac{dm_0}{\hat{m}_0} \right)^2 + \left(\frac{dm_f}{\hat{m}_f} \right)^2 \right] \\ &= \frac{1}{\sigma^2} \left[\frac{1}{\hat{m}_0} + \frac{1}{\hat{m}_f} \right] \\ \text{Var}(n)_{photon} &\approx \frac{1}{\hat{m}_0 \sigma^2} \left[1 + e^{-\hat{n}\sigma} \right] \end{aligned} \quad (3.19)$$

where the subscript ‘*photon*’ refers to the fact that this is the contribution to the noise on the image due purely to variation in photon number, i.e. not including variation in the atom number density itself. This equation is not used to calculate the theoretical photon shot noise, however it is instructive as the real equation (3.20) derived in the next section involves a function which is not expressible in simple algebraic form.

3.4.3 Complete model

If we include the corrections of section 3.2.2 we find that we still have

$$E(m_0) = \text{Var}(m_0) = \hat{m}_0.$$

and

$$E(m_f) = \text{Var}(m_f) = \hat{m}_f.$$

but this time, \hat{m}_f is related to \hat{m}_0 by the inverse function of equation (3.18);

$$\begin{aligned} n(x, y) &= \frac{1}{\sigma_0} \left[\frac{m_0 - m_f}{m_{sat}} + L \ln \left(\frac{\alpha m_0}{m_f + (\alpha - 1)m_0} \right) \right] \\ &= f(m_0, m_f, L) \end{aligned}$$

so that

$$\hat{m}_f = f^{-1}(\hat{n}, \hat{m}_0, L),$$

but in general f^{-1} is not expressible in simple algebraic form. Nonetheless, we may continue keeping in mind that we may need some computational tricks to calculate \hat{I}_f . Again using

propagation of errors, we see that

$$\begin{aligned}
 (dn)_{photon}^2 &= \left[\left(dm_0 \cdot \frac{\partial}{\partial \hat{m}_0} \hat{n} \right)^2 + \left(dm_f \cdot \frac{\partial}{\partial \hat{m}_f} \hat{n} \right)^2 \right] \\
 &= \frac{1}{\sigma_0^2} \left[\hat{m}_0 \left(\frac{1}{m_{sat}} + \frac{L}{\hat{m}_f + (\alpha - 1) \hat{m}_0} \right)^2 + \hat{m}_f \left(\frac{1}{m_{sat}} + \frac{L \hat{m}_f}{(\hat{m}_f + (\alpha - 1) \hat{m}_0) \hat{m}_0} \right)^2 \right] \\
 \text{Var}(n)_{photon} &\approx \frac{1}{\sigma_0^2} \left[\hat{m}_0 \left(\frac{1}{m_{sat}} + \frac{L}{\hat{m}_{af}} \right)^2 + \hat{m}_f \left(\frac{1}{m_{sat}} + \frac{L \hat{m}_f}{\hat{m}_{af} \hat{m}_0} \right)^2 \right]
 \end{aligned} \tag{3.20}$$

where on the last line I have defined the shorthand⁸ $\hat{m}_{af} = \hat{m}_f + (\alpha - 1) \hat{m}_0$. By taking the limit $m_{sat} \rightarrow \infty$ and inserting $\alpha = 1$ so that once again $\hat{m}_f = \hat{m}_0 e^{-\hat{n}\sigma}$, we find that after some algebra⁹ we recover equation (3.19). The equation (3.20) is used to calculate the theoretical photon shot noise in the experiment, and can be seen in action in the results of Chapter 5.

3.4.4 Effect of classical fringes

Suppose the effect of a particular fringe (which could be caused by a speck of dust, a scratch, or the edge of a mirror, etc.) is to relocate some light¹⁰ δI from outside where the atoms are (in the picture we take with the camera), to on top of where they are.

$$I \rightarrow I + \delta I \tag{3.21}$$

Assume also that any classical fringes are small compared to the total amplitude of the light, i.e.

$$\delta I \ll I.$$

It is clear that any fringes that occur before the atoms (before point *A* in Figure 4.1) will not affect the calculated atom distribution, as they will be properly accounted for by the treatment of equation (3.18). However, any fringes that occur after the light has passed through the atoms (after point *B* in Figure 4.1) will effect a change in the calculated atom distribution. Let us calculate that change in the simple imaging model of section 3.2.1. Equation (3.4) gives us

$$n_{calc} = \frac{1}{\sigma} \ln \left(\frac{I_0 + \delta I}{I_f + \delta I} \right)$$

⁸This is the same as in section 3.2.2, but is a shorthand here simply because I_{af} must be calculated from I_f and I_0 .

⁹Mainly consisting of setting $\sigma = \sigma_0/L$.

¹⁰For example, locally the fringe could be described by $\delta I \approx \delta \times \cos^2(k_x x + k_y y)$ where $\mathbf{r} = [x, y]$ are the coordinates perpendicular to the propagation direction of the light, and \mathbf{k} is a wave vector representing the fringe. The \cos^2 is chosen so that the light intensity is only increased by the fringe. This is only an instructive model, and not a proper treatment of the effects of classical fringes.

and we know that before the fringes occurred $I_f = I_0 e^{-n\sigma}$ so

$$\begin{aligned} n_{calc} &= \frac{1}{\sigma} \ln \left(\frac{I_0 + \delta I}{I_0 e^{-n\sigma} + \delta I} \right) \\ &= \frac{1}{\sigma} [\ln(I_0 + \delta I) - \ln(I_0 e^{-n\sigma} + \delta I)] \\ &\approx \frac{1}{\sigma} \left[\ln(I_0) + \frac{\delta I}{I_0} - \ln(I_0 e^{-n\sigma}) - \frac{\delta I}{I_0 e^{-n\sigma}} \right] \\ &= n - \frac{\delta I}{\sigma I_0} (e^{n\sigma} - 1) \end{aligned}$$

and we will calculate fewer atoms than we should. Note that the fringing on our atom distribution will be proportional to the original fringes, and it will increase with optical depth $e^{n\sigma}$ and detuning Δ (which will come through in σ). In the full model of section 3.2.2 we will arrive at the same conclusion, as the δI 's in the intensity correction term will cancel. A proper treatment of diffraction fringes would also allow for the possibility of fringes which remove light from the area where the atoms are, and this would cause us to calculate more atoms than we should.

Therefore, as one would expect, we can achieve better data by removing fringes from our imaging system (by cleaning, realigning etc.) before taking measurements.

3.5 Sources of blurring

We could now construct a model of what we expect to see if we were to image a cloud of fixed, stationary atoms. Unfortunately nature is rarely so kind: the main issue we have remaining to deal with is blurring of the image. The pixels on each image can be thought of as independent atom detectors, each one measuring a number of atoms N_i . If there is a mechanism which causes the atomic image to be spread over a fraction $\epsilon < 1$ of a pixel length in a given orientation, then neighbouring pixels in that direction are no longer independent samples of the atom distribution. A simple model of blurring says they are now correlated by

$$N_i \rightarrow \frac{1}{1+\epsilon} N_i + \frac{1}{2} \frac{\epsilon}{1+\epsilon} (N_{i-1} + N_{i+1}). \quad (3.22)$$

This can be seen by considering how a blurred atom occupying a length ϵ , and at least partially occupying a given pixel N_i contributes to its neighbouring pixels. By symmetry, the contribution from neighbouring pixels to a given pixel (3.22) will be the same. Consider a length ϵ anywhere in between positions a and b in Figure 3.2. It is clear that summing over all possible positions in this region will lead to a contribution proportional to $\epsilon/2$ ending up in each of N_{i-1} and N_i (as the total distance traversed by the left edge of the blur is ϵ). From position b to c , the whole contribution (proportional to $1 - \epsilon$) will go to N_i , and from position c to d we have the same situation as we had initially, only this time a contribution of $\epsilon/2$ goes to both N_i and N_{i+1} . Adding all the contributions to each pixel, and normalising all of them by the total distance $1 + \epsilon$ traversed by an edge of the blur from positions a to d , we arrive at (3.22).

In the case where the atomic image is spread over $\epsilon > 1$ pixel lengths, we have $n - 1 < \epsilon < n$, $n \in \{2, 3, 4, \dots\}$, and a little further work will show that the function (3.22) becomes

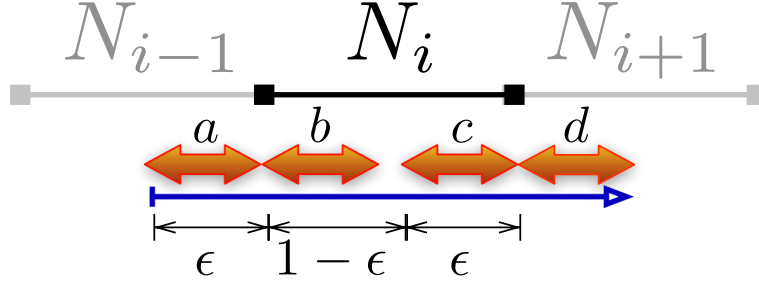


Figure 3.2: Considerations leading to (3.22). The orange, thick double headed arrows represent a blurred atom, and could be in any of positions a, b, c or d .

$$N_i \rightarrow \frac{1}{n(2\epsilon + 1 - n)} \left\{ \epsilon N_i + \left(\sum_{k=1}^{n-1} \left[\epsilon - k + \frac{1}{2} \right] N_{i \pm k} \right) + \frac{1}{2} [\epsilon - n + 1] (N_{i-1} + N_{i+1}) \right\}. \quad (3.23)$$

This does not reduce to (3.22) when $n = 1$ as it contains terms dependent upon $\epsilon > 1$. We now examine some different sources of blurring and the extent to which they will blur the image.

3.5.1 Gravity

As the atoms fall under gravity, they experience an acceleration¹¹ of $g \approx 9.79 \text{m/s}^2$. After a ballistic expansion of time τ they have a velocity of

$$u = g\tau$$

and so the distance they travel while being illuminated from a laser with a pulse time t is

$$\begin{aligned} s_{grav} &= g\tau t + \frac{1}{2}gt^2 \\ &= gt \left(\tau + \frac{t}{2} \right). \end{aligned} \quad (3.24)$$

However, the atoms will spend more time closer to their initial position and less time at their final position, so to account for this we average over the exposure time:

$$\begin{aligned} \langle s_{grav} \rangle &= \frac{1}{t} \int_0^t gt' \left(\tau + \frac{t'}{2} \right) dt' \\ &= \frac{gt}{2} \left(\tau + \frac{t}{3} \right) \end{aligned} \quad (3.25)$$

which is roughly half of the distance in (3.24). Typical values are t from 1 to $100\mu\text{s}$ and τ from 5 to 30ms, giving $\langle s_{grav} \rangle \approx 1$ or $2\mu\text{m}$. The distance blurred (as measured by equation (3.25)) is plotted on the left of Figure 3.3.

¹¹In Canberra.

3.5.2 Temperature

Blurring due to temperature for thermal atoms is given by

$$k_B T = \frac{1}{2} m \mathbf{v}^2$$

where v is taken to be the speed in a plane parallel to the imaging plane (i.e. $\mathbf{v}^2 = v_x^2 + v_y^2$). Thus a typical distance blurred is given by

$$\begin{aligned} s_{therm} &= \int_0^t |\mathbf{v}| dt \\ &= t \sqrt{\frac{2k_B T}{m}} \end{aligned}$$

where t is the imaging pulse time. For rubidium with a typical $t \approx 30 \mu\text{s}$ and $T \approx 1 \mu\text{K}$, we have $s_{therm} \approx 0.5 \mu\text{m}$.

3.5.3 Photon recoil in the imaging plane

The atoms cast a shadow on the imaging laser beam because they absorb, and then spontaneously emit photons from it. Each absorption will be a kick in the direction of the beam. Each spontaneous emission can be considered a step in a random walk in velocity, with a step length of the recoil velocity

$$v_{rec} = \frac{\hbar k}{m}.$$

The number of steps in the walk will be given by the photon scattering rate of the atoms, and the pulse time t

$$\begin{aligned} N &= R_{scatt} t \\ &= \frac{\Gamma}{2} \frac{I/I_{sat}}{\left(\frac{2\Delta}{\Gamma}\right)^2 + 1 + I/I_{sat}} t. \end{aligned}$$

As a random walk in 1, 2 or 3 dimensions with N steps of length l is expected to end up a root-mean-square distance¹² of $l\sqrt{N}$ away from its starting position [37], we can expect the final speed in a plane parallel to the imaging plane will be given by

$$\langle v_N^2 \rangle = \frac{2\hbar^2 k^2}{3m^2} \frac{\Gamma t}{2} \frac{I/I_{sat}}{\left(\frac{2\Delta}{\Gamma}\right)^2 + 1 + I/I_{sat}} \quad (3.26)$$

¹²Although the average r.m.s. distance $\langle v^2 \rangle$ is analytically calculable, the average distance $\langle v \rangle$ is not. Hence $\langle v_N^2 \rangle$ appears in (3.26).

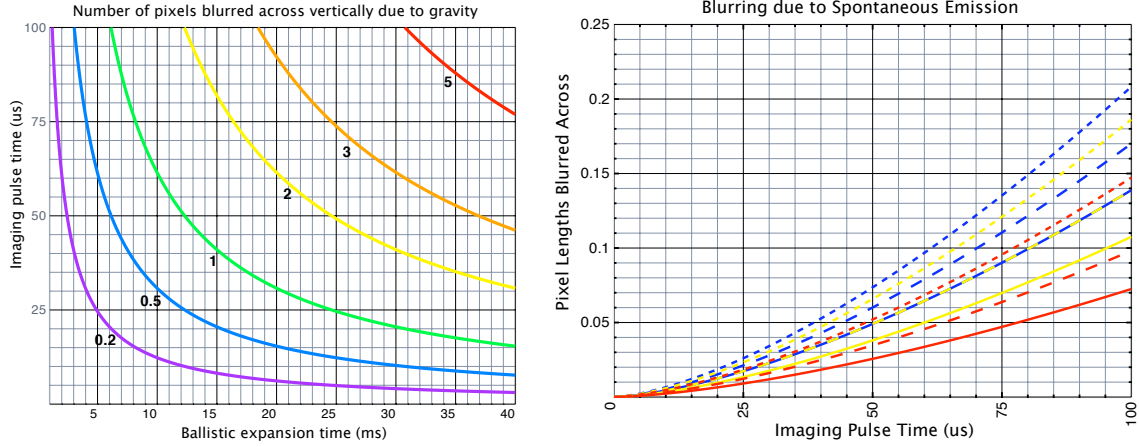


Figure 3.3: **Left:** Pixel lengths each atom is blurred over due to gravitational acceleration. Better resolution is achieved at shorter expansion times and shorter imaging pulses. **Right:** How many pixel lengths does the random walk from spontaneous emission push the atoms? Intensity is given by $I/I_{sat} = 0.5, 1, 3$ which are respectively solid line, large dashes, and small dashes. Detuning in half-linewidths is given by $2\Delta/\Gamma = 0, 1, 2$ which are respectively blue, yellow and red.

where the factor of $2/3$ is to ignore the component of this motion in the z (imaging axis) direction. So a generous estimate of the distance traveled during the imaging pulse is

$$\begin{aligned} s_{rec} &= \int_0^t |v_N| dt' \\ &= \int_0^t \frac{\hbar k}{\sqrt{3m}} \sqrt{\Gamma t' \frac{I/I_{sat}}{\left(\frac{2\Delta}{\Gamma}\right)^2 + 1 + I/I_{sat}}} dt' \\ &= \frac{2\hbar k}{3\sqrt{3m}} \sqrt{\frac{\Gamma t^3}{\frac{I_{sat}}{I} \left[\left(\frac{2\Delta}{\Gamma}\right)^2 + 1\right] + 1}} \end{aligned} \quad (3.27)$$

which will be maximum in the limit that $I \gg I_{sat}$,

$$s_{rec \ max} = \frac{2\hbar k}{3\sqrt{3m}} \sqrt{\Gamma t^3}$$

which, for ^{87}Rb with values from table 2.1, is

$$s_{rec \ max} = 0.7245 t^{3/2} \quad (\text{m}, t \text{ in } \text{s})$$

and putting this in pixel lengths (including the effect of magnification by a factor of $M = 2.14$) $s' = s \times M/\text{pixel}$

$$s'_{rec \ max} = 2.404 \times 10^{-4} \times t^{3/2}. \quad (\text{pixels}, t \text{ in } \mu\text{s})$$

This is plotted in Figure 3.3.

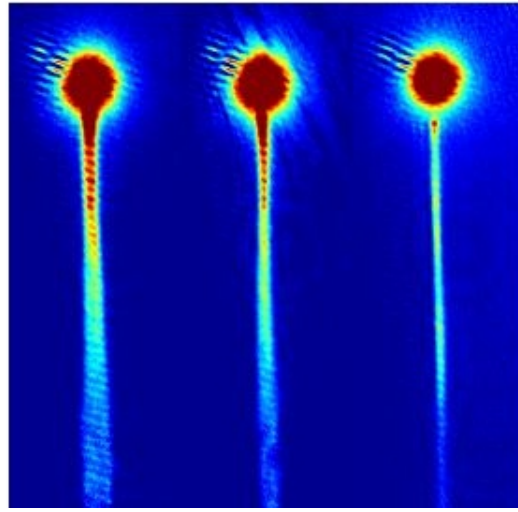


Figure 3.4: An image that was taken in 2006. It shows the atom laser in action. The classical fringes can be clearly seen and would dominate the noise on the image.

3.5.4 Diffraction limit of optics

The diffraction limit to the resolution of an optical system is given by the Rayleigh criterion,

$$s_{diff} = 1.22 \times \lambda \frac{f}{D}$$

where f and D are the focal length and diameter of the lens used and λ is the wavelength of the light. Using $f = 10\text{cm}$ and $D = 5\text{cm}$ (measured from the lens) gives a diffraction limit of

$$\begin{aligned} s_{diff} &= 1.22 \times 780.24 \times 10^{-9} \times \frac{10}{5} \\ &= 1.904 \mu\text{m} \text{ or } 0.63 \text{ pixels} \end{aligned}$$

which is a large fraction of the pixel length at the atom cloud¹³, $3.01\mu\text{m}$. So in the experimental regime of small imaging pulse time and ballistic expansion time, with high detuning and low intensity, the diffraction limit will be the dominant source of blurring.

3.6 Old Images

For comparison, an absorption image is shown in Figure 3.4 which was taken before I started my project. Classical fringes are clearly seen on the image. It is pertinent to mention that an important part of this project was identifying and removing all the sources of these types of classical noise, including cleaning of optical elements, re-aligning so as to avoid interference fringes, and replacing or removing elements which introduced too much noise via scratches, defects, aberrations, fringes etc.

¹³which is the pixel length P ($6.45\mu\text{m}$ in this experiment) divided by the magnification M (2.14 in our setup).

The New System

Given all of the considerations from the previous chapter, we set out to construct a new imaging system capable of observing atomic shot noise. This chapter describes the new imaging system and its calibration, along with some calibrative measurements of a new Ioffe trap which was installed concurrently.

4.1 Imaging setup

The path of the imaging beam in our experiment is illustrated in Figure 4.1. The optical fibre outputs linearly polarised light which is divergent, and so must be re-collimated by a lens. From here the beam reflects off a mirror (so as to avoid blocking one of the 3D MOT beams) and passes through a quarter-waveplate which circularly polarises the light, so it will drive the closed transition illustrated in Figure 2.1. The beam enters the glass cell of the vacuum chamber where the cold atom cloud is located, passes through the atoms, and exits the other side of the glass cell. The image of the atoms is focused by a 10 cm focal length lens onto a CCD camera, with a magnification factor of approximately 2. An accurate measurement of the magnification of the image is presented in section 4.3.1. The imaging path is on a slight angle (about 7°) so as to avoid the interferometer setup which is occupying the perpendicular alignment. The image was brought into focus by aligning according to the lens equation

$$\frac{1}{f} = \frac{1}{d_i} + \frac{1}{d_o}$$

and then crisp focus was achieved by calibration with the cloud itself. If the imaging light is perfectly resonant then the maximum optical depth and the smallest cloud diameter will be achieved when the cloud is in focus [5], so the position of the camera was adjusted to achieve the maximum possible optical depth (OD) and the smallest possible Airy disk in the image of a small cloud. However this method does not accurately hone in upon the imaging plane as lensing at slight detunings from resonance will change the size of the cloud's image, so further focusing is necessary. By detuning the imaging light to either side of the atomic resonance we can exploit the lensing effect of a dense atom cloud [5], which causes the observed OD to increase or decrease depending upon the position of the camera. The imaging plane is found where the detuned peak OD curve intersects the resonant peak OD curve. This technique involving detuning is not required with dispersive imaging techniques as they can measure very large atomic densities [44], and so focusing can be achieved in-trap on very small dense clouds.

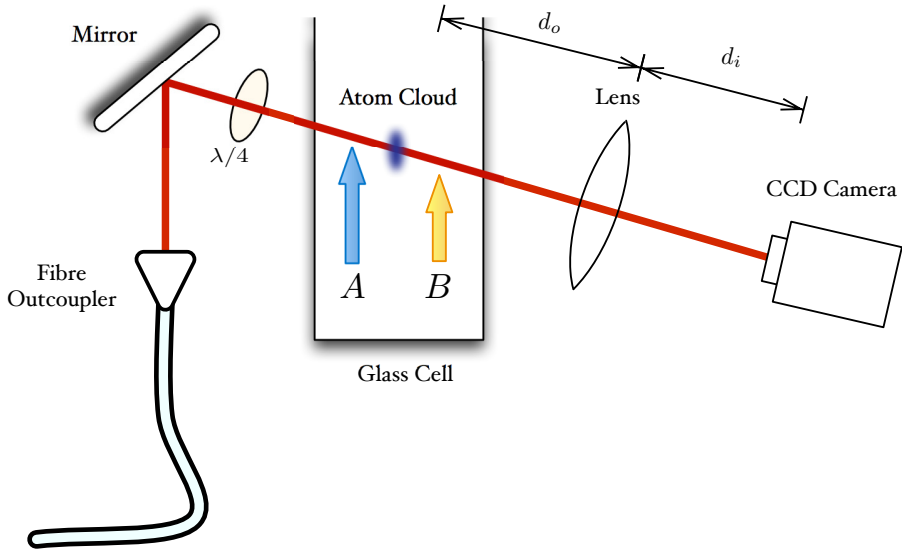


Figure 4.1: Diagram of the minimal imaging setup. The image distance $d_i = 30\text{ cm}$ and object distance $d_o = 15\text{ cm}$ will determine the magnification of the image, $M = -d_i/d_o = -2$, where the minus sign implies image inversion. Intensity fluctuations due to fringes, scratches and dust which occur before point A (before the atoms) will not affect our calculations, but those occurring after point B will.



Figure 4.2: The camera used was a Point Grey Research *Grasshopper*.

4.2 Camera Calibration

CCD cameras come in a huge variety of prices and specifications. Often, however, the specifications of the camera (in all price ranges from \$1000 to \$50,000) do not match those alluded to in the documentation, or fail to be documented at all. Thus we must measure all the relevant parameters of the camera system accurately. The camera chosen was a Point Grey Research Grasshopper, and its important characteristics are listed in Table (4.1) below. This camera was chosen for its claimed quantum efficiency of 35% and 14 bit digitization, for a low price of \$2000. Of these three values, only the price was accurate. Other, more expensive (see price bracket above) cameras were also tested, and this one proved to be the best available.

Name	Value	Source
Model	Grasshopper 14S5	[45]
CCD chip	Sony® ICX285 2/3" progressive scan CCD	[45]
Array size	1384(H)×1036(V)	[45]
Pixel dimensions	6.45μm×6.45μm	[45]
Max. bit depth	4096=12 bit	Experiment
System gain s	0.240 ± 0.002	Experiment
Quantum efficiency @ 780nm	17.4%	Experiment
Well depth	17,000e ⁻	Experiment
Dark count	<3 counts per 0.1ms per pixel	Experiment

Table 4.1: Parameters of the PGR Grasshopper camera used in the experiment.

4.2.1 System gain

Assuming that we have the special situation in which the number of electrons X in each well is independently poissonian distributed with mean and variance a ,

$$X \sim \text{Poi}(a)$$

then the count at each pixel on the digitised image is $Y = sX$ (where s , the system gain, is a multiplicative factor introduced at the analog to digital conversion stage) which has

$$\begin{aligned} \text{E}(Y) &= \text{E}(sX) \\ &= s\text{E}(X) \\ &= sa \end{aligned}$$

and

$$\begin{aligned} \text{Var}(Y) &= \text{Var}(sX) \\ &= s^2\text{Var}(X) \\ &= s^2a. \end{aligned}$$

So, we may find the system gain of the camera by taking

$$\frac{\text{Var}(Y)}{\text{E}(Y)} = s$$

or more properly¹, taking the gradient s of the line of best fit of the equation

$$\text{Var}(Y) = s\text{E}(Y) + c$$

The intercept c is a measure of the systematic error in the measurement, in this case it could be readout noise, dark noise, or a variance floor imposed by curvature of the illumination. Experimentally, a flat-field image will have the statistical properties we require². Flat-

¹To avoid any systematic error in the measurement, as is done in the literature [46].

²This is because a thermal light source with M modes will have a variance in photon number n of $\text{Var}(n) = \langle n \rangle + \langle n \rangle^2/M$ [47, 48]. As the number of modes increases (to a very large number for an incandescent bulb), the variance approaches that for Poissonian statistics.

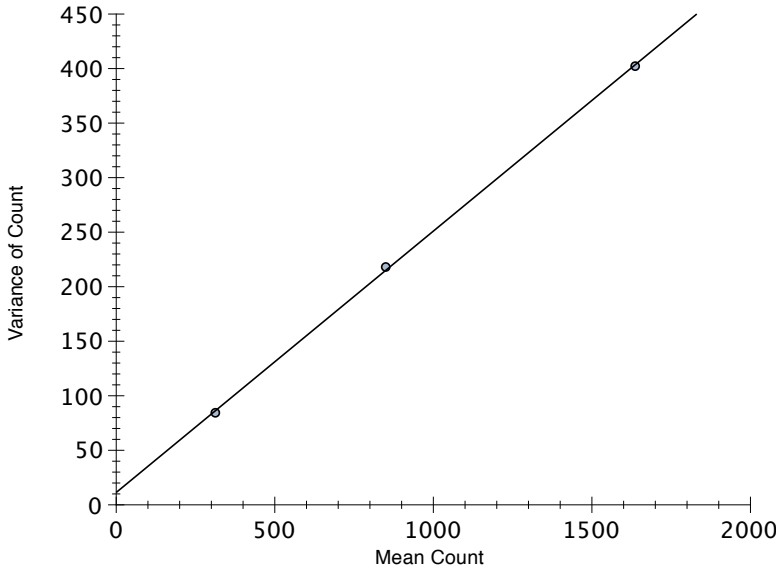


Figure 4.3: The system gain is measured as the gradient of this plot of variance vs. mean count number for each pixel on flat field images. Each data point is an average from all of 1036×1384 pixels on 100 images, so the standard error on each data point is of the order of 10^{-6} to 10^{-8} in both directions, and has not been drawn in. The system gain was found to be 0.240 ± 0.002 .

field images were generated by shining a torch directly at the camera, while covering the aperture with a variable number of sheets of blank white paper to diffuse the light and vary the intensity. The results can be seen in Figure 4.3. Each data point is given by the mean and variance of Y , averaged over 1036×1384 pixels on 100 images taken with that thickness of paper. Two brighter data points were excluded from analysis for the following reasons; with only one or two sheets of paper covering the aperture, variation in the optical thickness of the paper will increase the variance, and the light from the torch has not diffused enough for the image to be considered flat, again increasing the variance.

The system gain was found by this method to be 0.240 ± 0.002 counts per electron, and the intercept was found to be 11.3 ± 2.5 counts² per electron, where the errors stated are the errors in the linear least-squares fit. Using the system gain and the maximum possible count (4096) we can put a lower bound on the well depth,

$$\begin{aligned}
 \text{Well depth} &\geq \frac{(\text{max count})}{s} \\
 &= 4096 / (0.240 \pm 0.002) \\
 &= 17066 \pm 142 \\
 &\approx 17,000 \text{ electrons.}
 \end{aligned}$$

Of course the well depth may be greater than this, to allow some pixels to be saturated without blooming into adjacent pixels. In fact, another camera which uses the same Sony ICX285 CCD chip [49] quotes the well depth at 15,000 electrons, but this is of course only the maximum number which can be read out, which is an engineering decision to avoid blooming and not an inherent property of the CCD array.

4.2.2 Quantum efficiency

The quantum efficiency is defined as the fraction of photons hitting a pixel which result in an electron in the well. It can be determined by calibrating the intensity for a given exposure time to the number of counts on an image. Images such as on the left of Figure 4.4 were taken for various total imaging laser powers P and camera exposure times t . The sum of the pixel counts in the rectangular Region Of Interest ($A_{ROI} = d_1 d_2$ where d_i are in pixels) for the image were divided by the number of pixels in the ellipse of interest (defined by $A_{ellipse} = \pi d_1 d_2 / 4$,³ see Figure 4.4) to arrive at the average count per pixel⁴ $\langle \phi \rangle$:

$$\langle \phi \rangle = \frac{4}{\pi d_1 d_2} \cdot \sum_{\text{all pixels in ROI}} \phi_i. \quad (4.1)$$

This was plotted against the total power in the imaging beam $P(\mu\text{W})$ and the exposure length of the image $t(\text{ms})$ in the right of Figure 4.4. A least squares fit of the form

$$\langle \phi \rangle = \alpha_1 \cdot P(\mu\text{W}) \cdot t(\text{ms}) + \alpha_2$$

was performed which yielded $\alpha_1 = 1670 \pm 5$ and $\alpha_2 = 3 \pm 2$. The value of α_2 was thereafter discarded as insignificant, $\alpha_2 \approx 0$ as its contribution is small and probably largely due to the inclusion of the dark image corners in the sum in equation 4.1. The conversion between the total power in the imaging beam $P(\mu\text{W})$, and the power incident upon one pixel $p(\mu\text{W})$ is the ratio of the areas which they cover;

$$\begin{aligned} p(\mu\text{W}) &= P(\mu\text{W}) \times \frac{A_{pixel}}{A_{ellipse}} \\ &= P(\mu\text{W}) \times \frac{4}{\pi d_1 d_2} \end{aligned}$$

Thus each pixel's count may be converted to an intensity at the CCD chip of

$$\begin{aligned} I(\text{mW cm}^{-2}) &= \frac{p(\text{mW})}{A_{pixel}(\text{cm}^2)} \\ &= \frac{10^{-3} P(\mu\text{W})}{A_{pixel}(\text{cm}^2)} \times \frac{4}{\pi d_1 d_2} \\ &= \frac{\phi}{\alpha_1 t(\text{ms}) A_{pixel}(\text{cm}^2) \times 10^3} \times \frac{4}{\pi d_1 d_2} \\ &= 1.46 \times 10^{-5} \times \frac{\phi}{t(\text{ms})} \end{aligned}$$

with a 0.4% error propagated from α_1 . The unusual units have been chosen because they are convenient and common units for intensities relevant to atom-light interactions⁵.

The quantum efficiency can now be calculated by the ratio of the number of electrons

³The root mean square radius was calculated to be $\sqrt{d_1 d_2} / 4 = 353.9 \text{ px}$.

⁴This assumes that the dark pixels in each of the corners contribute little to the image.

⁵For example the saturation intensity for the $5^2 S_{1/2} \rightarrow 5^2 P_{3/2}$ ^{87}Rb transition $|F = 2, m_F = 2\rangle \rightarrow |F = 3, m_F = 3\rangle$ is $I_{sat} = 1.67 \text{ mW cm}^{-2}$ [38]. Since $\langle \phi \rangle_{max} = 4096$ and $t \approx 0.1 \text{ ms}$ this gives us an intensity range of 0 to $1.4 \times I_{sat}$ at the camera, which, with a magnification of ≈ 2 means an intensity of $2.8 \times I_{sat}$ at the position of the atoms. This can be increased by going to shorter exposure times.

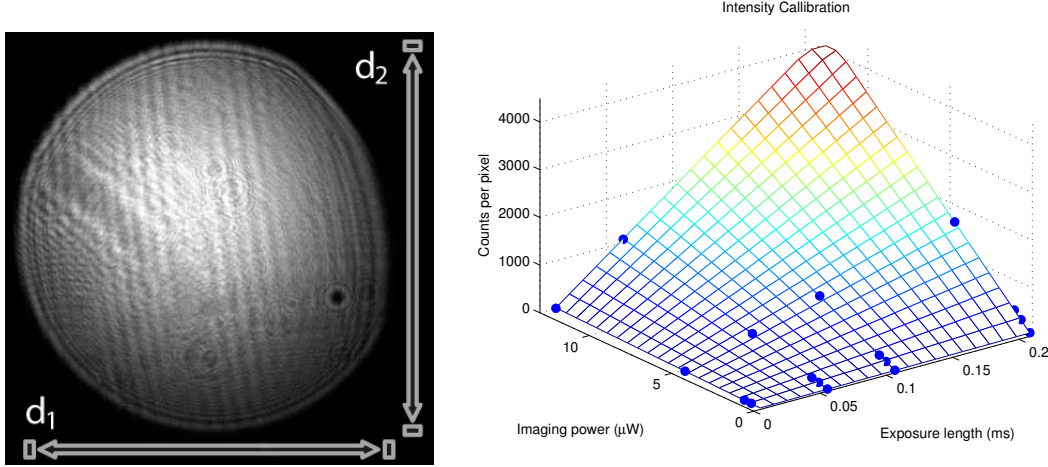


Figure 4.4: To calibrate the intensity of the light incident upon the camera, the count per pixel was measured from images (left) for various total imaging laser powers P and camera exposure times t . The mesh (right) represents the fitted equation $\text{counts} = \alpha_1 \cdot P(\mu\text{W}) \cdot t(\text{ms}) + \alpha_2$. The fit gave $\alpha_1 = 1670 \pm 5$ and $\alpha_2 = 3 \pm 2$. The mesh has a ceiling at 4096 which is the maximum count on a pixel. Images with higher counts per pixel were saturated in parts, and were excluded from the analysis.

m sitting in each pixel's well to the number of photons n incident on that pixel:

$$\begin{aligned}
 Q.E. &= \frac{m}{n} \\
 &= \frac{\langle \phi \rangle / s}{pt/E_{\text{photon}}} \\
 &= \frac{\langle \phi \rangle E_{\text{photon}}}{10^{-6}P(\mu\text{W})10^{-3}t(\text{ms})s} \times \frac{\pi d_1 d_2}{4} \\
 &= \frac{\alpha_1 \times 10^9}{s} \times \frac{hc}{\lambda} \times \frac{\pi d_1 d_2}{4} \\
 &= 0.174 \text{ or } 17.4\%
 \end{aligned}$$

This result is about half of the Q.E. recorded in the data sheet for a similar camera with the same ICX285 CCD chip [49].

4.2.3 Dark counts

Dark counts and readout noise were measured for various exposure times and then ignored as insignificant. Combined, they contributed approximately 3 counts to each pixel during the $100\mu\text{s}$ exposure which we used.

4.3 Atom Cloud Calibration

The properties of the atom cloud are extracted from images, so it is pertinent that we know quantitatively what those images are telling us. This section details the calibration necessary to make accurate measurements.

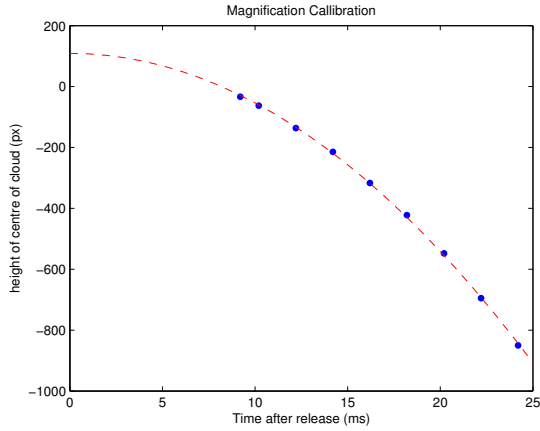


Figure 4.5: The magnification of the imaging setup was measured to be 2.14 ± 0.02 by dropping a cloud of atoms and taking images at times t after release. The magnification was determined by a parabolic fit to the atoms' fall under gravity, measured by the centre of a gaussian fit to the cloud.

4.3.1 Magnification of Imaging setup

The magnification of our imaging setup (nominally 2) was determined by timing the fall of an atom cloud released from the trap. The cloud was dropped by radio-frequency outcoupling a small atom pulse, t milliseconds before taking an image. The height of the centre of the atom cloud was measured by fitting a gaussian to each image. Finally, the magnification was determined by fitting the parabola

$$h = h_0 - \frac{1}{2}at^2$$

to the atom's vertical trajectory as is shown in Figure 4.5. The magnification was calculated to be 2.14 ± 0.02 by the equation

$$M = \frac{ap}{g}$$

where a is the fit parameter for acceleration in px/s^2 , p is the pixel size in m and $g = 9.79 \text{m/s}^2$ is the acceleration due to gravity.

Other methods have been proposed to measure the magnification of the imaging system, such as the crossed beam method. This involves splitting of a fraction of the imaging beam which is also directed at the location of the atoms. The beams cross at this location and so act as separate rays diverging from the object position. If the second beam is aligned so as to overlap the first on the CCD array, an interference pattern will be observed which can be used to measure the angle at which the beams converge to the CCD. The ratio of this angle to the angle at which the beams intersect at the atom position is the magnification of the imaging setup. For details, see [44]. This would be required if we were to measure g using this setup.

4.3.2 Harmonic trap frequencies

We must also measure the properties of the Ioffe trap in which the cold atoms reside. In the approximation that the Ioffe trap is harmonic, the only parameters that we need to measure are the trap frequencies - the oscillation frequencies of a classical particle in the trap - in each direction. The radial trap frequency $f_r = \frac{\omega_r}{2\pi}$ was measured by applying an oscillating

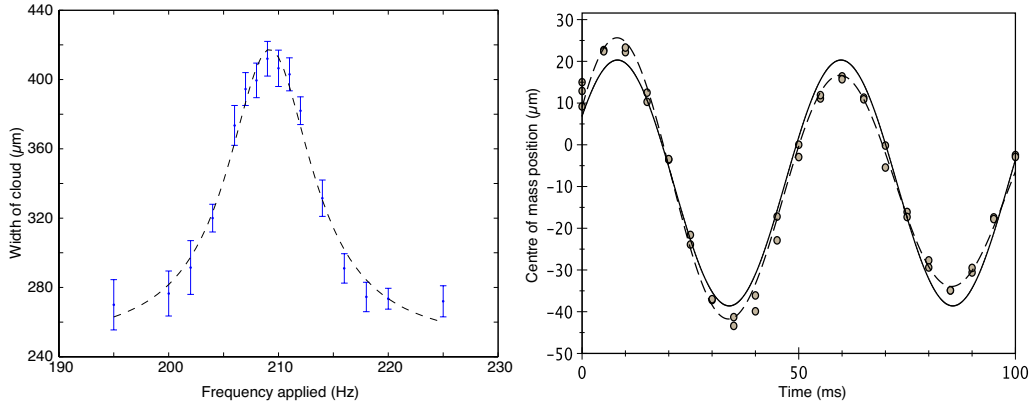


Figure 4.6: **Left:** The radial trapping frequency was measured to be 209.2 ± 0.3 Hz by resonantly heating the cloud with an oscillating magnetic field with frequency f . In this graph the average width of the cloud (measured as standard deviation of a gaussian fit) after ballistic expansion is plotted against f . The fitted curve is a Lorentzian lineshape used to measure the centre of the resonance. **Right:** The axial trapping frequency was measured to be 19.4 ± 0.1 Hz by giving the atom cloud a ‘kick’ and then allowing it to slosh backwards and forwards until a time t later when the trap was turned off. In this graph the horizontal displacement of the cloud after ballistic expansion is plotted against t . Both axes are measured against arbitrary reference points. The fitted curves are a sine wave (full) and an exponentially decaying sine wave (dotted). The decay is attributed to coupling to the orthogonal oscillation modes in the trap. Two measurements have been taken at each time t to give an idea of the uncertainty.

magnetic field at a variable frequency f , using the RF outcoupling coil already in position. The cloud experienced a peak in temperature due to resonant transfer of energy to the atoms when the applied frequency f matched the trap parameter f_r . Temperature was measured by width of a Gaussian fit to the cloud, and the result is plotted in Figure 4.6. A Lorentzian lineshape has been fit to accurately determine the centre of the resonance, and thus the radial trapping frequency was measured to be 209.2 ± 0.3 Hz.

The axial trap frequency $f_a = \frac{\omega_a}{2\pi}$ was measured by applying a short pulse from a second solenoid in the axial direction, causing in-trap oscillation. The frequency of this oscillation was measured by releasing the atoms from the trap a time t later, and measuring the displacement in the x direction. In this way, the axial trap frequency was measured to be 19.4 ± 0.1 Hz, as is shown in Figure 4.6.

4.3.3 Temperature calibration

It is important to measure the temperature of an atom cloud properly as this provides the basis for number calibration, and it quantifies the thermal contribution to blurring.

4.3.3.1 Derivation of the Thermal Cloud Density

We begin by using a semi-classical treatment to evaluate of the density of atoms in a thermal cloud

$$\rho_{th}(\mathbf{r}) = \frac{N - N_0}{V}$$

at temperatures close to the transition temperature, where N is the total number of atoms in volume V and N_0 is the number of atoms in the condensate in the volume V . The Bose

distribution function for the number of atoms N_i occupying an eigenstate with energy ε_i is given by

$$N_i = \frac{1}{e^{(\varepsilon_i - \mu)\beta} - 1} \quad (4.2)$$

where the chemical potential μ is determined such that

$$N = \sum_i \frac{1}{e^{(\varepsilon_i - \mu)\beta} - 1}$$

is the total number of particles in the system. Following [50], we find the density by integrating (4.2) over $d^3\mathbf{p}/h^3$,⁶ with the explicitly semi-classical energy $\varepsilon_{\mathbf{p}}(\mathbf{r}) = \frac{\mathbf{p}^2}{2m} + V(\mathbf{r})$. Thus

$$\rho_{th}(\mathbf{r}) = \frac{1}{h^3} \int_{-\infty}^{\infty} \int_{-\infty}^{\infty} \int_{-\infty}^{\infty} \frac{d^3\mathbf{p}}{e^{\left(\frac{\mathbf{p}^2}{2m} + V(\mathbf{r}) - \mu\right)\beta} - 1}. \quad (4.3)$$

But, before launching into this integral, it is important to realise that what we image is this thermal density *after it has undergone ballistic expansion for a time t*. Equation (4.3) represents only the in-trap density. This means that we must evaluate the potential V at the position \mathbf{r}_0 when the particle was in-trap, and then integrate over all possible starting positions for the same final position. Realizing that in the absence of collisions,

$$\mathbf{p} = \frac{m}{t}(\mathbf{r} - \mathbf{r}_0)$$

we can integrate over equation (4.3) like so,

$$\begin{aligned} \rho_{th}(\mathbf{r}, t) &= \frac{1}{h^3} \iiint d^3\mathbf{r}_0 \iiint d^3\mathbf{p} \frac{\delta^3(\mathbf{r} - \mathbf{r}_0 - \mathbf{p}\frac{t}{m})}{e^{\left(\frac{\mathbf{p}^2}{2m} + V(\mathbf{r}_0) - \mu\right)\beta} - 1} \\ &= \frac{1}{h^3} \int_{-\infty}^{\infty} \int_{-\infty}^{\infty} \int_{-\infty}^{\infty} d^3\mathbf{p} \frac{1}{e^{\left(\frac{\mathbf{p}^2}{2m} + V(\mathbf{r} - \frac{t}{m}\mathbf{p}) - \mu\right)\beta} - 1}. \end{aligned}$$

Taking a harmonic trapping potential

$$\begin{aligned} V(\mathbf{r}) &= \frac{m}{2} (\omega_x^2 x^2 + \omega_y^2 y^2 + \omega_z^2 z^2) \\ V\left(\mathbf{r} - \frac{t}{m}\mathbf{p}\right) &= \frac{m}{2} \sum_{i=1,2,3} \omega_i^2 \left(x_i - \frac{tp_i}{m}\right)^2 \\ &= \frac{m}{2} \sum_{i=1,2,3} \left[\omega_i^2 x_i^2 - \frac{2\omega_i^2 x_i t p_i}{m} + \left(\frac{\omega_i t p_i}{m}\right)^2 \right] \\ &= \sum_{i=1,2,3} \left[\frac{m\omega_i^2 x_i^2}{2} - \omega_i^2 x_i t p_i + \frac{\omega_i^2 t^2 p_i^2}{2m} \right] \end{aligned}$$

⁶This is because the phase-space volume element is $d^3\mathbf{p}d^3\mathbf{x}/h^3$, here we want a density so we leave out the $d^3\mathbf{x}$.

we see that

$$\begin{aligned}\rho_{th}(\mathbf{r}, t) &= \frac{1}{h^3} \iiint d^3\mathbf{p} \left[\exp \left(\beta \left(\frac{\mathbf{p}^2}{2m} + V(\mathbf{r} - \frac{t}{m}\mathbf{p}) - \mu \right) \right) - 1 \right]^{-1} \\ &= \frac{1}{h^3} \iiint d^3\mathbf{p} \left[\exp \left(\beta \left(-\mu + \sum_{i=1,2,3} \left[\frac{m\omega_i^2 x_i^2}{2} - \omega_i^2 x_i t p_i + (1 + \omega_i^2 t^2) \frac{p_i^2}{2m} \right] \right) \right) - 1 \right]^{-1}.\end{aligned}$$

Completing the square in the quadratic expression

$$\begin{aligned}&\frac{m\omega_i^2 x_i^2}{2} - \omega_i^2 x_i t p_i + (1 + \omega_i^2 t^2) \frac{p_i^2}{2m} \\ &= \frac{(1 + \omega_i^2 t^2)}{2m} \left(\frac{m^2 \omega_i^2 x_i^2}{1 + \omega_i^2 t^2} - \frac{2m\omega_i^2 x_i t p_i}{1 + \omega_i^2 t^2} + p_i^2 \right) \\ &= \frac{(1 + \omega_i^2 t^2)}{2m} \left(p_i - \frac{m\omega_i^2 x_i t}{1 + \omega_i^2 t^2} \right)^2 + \left(\frac{m\omega_i^2 x_i^2}{2} - \frac{m(\omega_i^2 x_i t)^2}{2(1 + \omega_i^2 t^2)} \right) \\ &= \frac{q_i^2}{\beta} + \frac{m\omega_i^2 x_i^2}{2} \left(1 - \frac{\omega_i^2 t^2}{1 + \omega_i^2 t^2} \right) \\ &= \frac{q_i^2}{\beta} + \frac{m x_i^2}{2} \left(\frac{\omega_i^2}{1 + \omega_i^2 t^2} \right)\end{aligned}$$

where I have substituted

$$q_i = \sqrt{\frac{1 + \omega_i^2 t^2}{2mk_B T}} \left(p_i - \frac{m\omega_i^2 x_i t}{1 + \omega_i^2 t^2} \right).$$

Thus

$$\begin{aligned}\rho_{th}(\mathbf{r}, t) &= \left(\prod_{i=1}^3 \frac{1}{\sqrt{1 + \omega_i^2 t^2}} \right) \left[\frac{2mk_B T}{h^2} \right]^{3/2} \\ &\quad \times \iiint d^3\mathbf{q} \left[\exp \left(-\beta \mu + \sum_{i=1,2,3} \left[q_i^2 + \frac{\beta m x_i^2}{2} \left(\frac{\omega_i^2}{1 + \omega_i^2 t^2} \right) \right] \right) - 1 \right]^{-1} \\ &= \left(\prod_{i=1}^3 \frac{1}{\sqrt{1 + \omega_i^2 t^2}} \right) \left(\frac{1}{\lambda_T \sqrt{\pi}} \right)^3 \int_{-\infty}^{\infty} \int_{-\infty}^{\infty} \int_{-\infty}^{\infty} d^3\mathbf{q} \frac{1}{e^{\mathbf{q}^2/\vartheta} - 1} \quad (4.4)\end{aligned}$$

where the thermal De Broglie wavelength is given by

$$\lambda_T = \sqrt{\frac{h^2}{2\pi m k_B T}} \quad (4.5)$$

and I have defined

$$\vartheta = \exp \left(\beta \left(\mu - \sum_{i=1}^3 \frac{m x_i^2 \omega_i^2}{2(1 + \omega_i^2 t^2)} \right) \right). \quad (4.6)$$

Using the Taylor series expansion

$$\frac{1}{\xi - 1} = \sum_{j=1}^{\infty} \xi^j \quad (4.7)$$

with $\xi = \vartheta e^{-\mathbf{q}^2}$ transforms equation (4.4) into

$$\begin{aligned} \rho_{th}(\mathbf{r}, t) &= \left(\prod_{i=1}^3 \frac{1}{\sqrt{1 + \omega_i^2 t^2}} \right) \left(\frac{1}{\lambda_T \sqrt{\pi}} \right)^3 \sum_{j=1}^{\infty} \vartheta^j \int_{-\infty}^{\infty} \int_{-\infty}^{\infty} \int_{-\infty}^{\infty} e^{-j\mathbf{q}^2} d^3 \mathbf{q} \\ &= \end{aligned} \quad (4.8)$$

$$\begin{aligned} \rho_{th}(\mathbf{r}, t) &= \left(\prod_{i=1}^3 \frac{1}{\sqrt{1 + \omega_i^2 t^2}} \right) \frac{1}{\lambda_T^3} \sum_{j=1}^{\infty} \frac{\vartheta^j}{j^{3/2}} \\ &= \left(\prod_{i=1}^3 \frac{1}{\sqrt{1 + \omega_i^2 t^2}} \right) \frac{1}{\lambda_T^3} \text{Li}_{3/2}(\vartheta). \end{aligned} \quad (4.9)$$

where $\text{Li}_s(z)$ is the polylogarithm function⁷

$$\text{Li}_s(z) = \sum_{n=1}^{\infty} \frac{z^n}{n^s}. \quad (4.10)$$

This expression is valid and most useful for temperatures around the condensation temperature T_c . Equation (4.9) will be used to derive the column density in the next section, to determine the temperature in section 4.3.3.5, and to derive the condensate fraction as a function of temperature in section 4.3.4.

4.3.3.2 Calculation of the Optical Thickness of the Thermal Distribution

For comparison with imaging we must find the 2D distribution of atoms after integration through all values along the imaging axis. This known as the column density and is given by

$$n_{th}(x, y, t) = \int_{-\infty}^{\infty} \rho_{th}(\mathbf{r}, t) dz \quad (4.11)$$

where z is the coordinate along the imaging axis. Labeling the normalisation constant in equation (4.9) as

$$\kappa = \left(\prod_{i=1}^3 \frac{1}{\sqrt{1 + \omega_i^2 t^2}} \right) \left(\frac{1}{\lambda_T} \right)^3$$

⁷Some properties of this function are mentioned for interest. By direct differentiation it can be seen that $\frac{d}{dx} \text{Li}_\gamma(x) = \frac{\text{Li}_{\gamma-1}(x)}{x}$. By evaluation it can also be seen that $\text{Li}_\gamma(1) = \sum_{n=1}^{\infty} \frac{1}{n^\gamma} = \zeta(\gamma)$, $\text{Li}_\gamma(0) = 0$, while it is also illustrative to know that the cases of $\gamma \in \{1, 0, -1, -2, \dots\}$ are elementary functions since $\text{Li}_1(x)$ is the Taylor series expansion of $-\ln(1-x)$.

and evaluating the integral,

$$\begin{aligned}
n_{th}(x, y, t) &= \int_{-\infty}^{\infty} \kappa \text{Li}_{3/2}(\vartheta) dz \\
&= \kappa \int_{-\infty}^{\infty} \text{Li}_{3/2} \left(\exp \left[\beta \left(\mu - \sum_{i=1}^3 \frac{mx_i^2 \omega_i^2}{2(1 + \omega_i^2 t^2)} \right) \right] \right) dz \\
&= \kappa \sum_{j=1}^{\infty} \int_{-\infty}^{\infty} \frac{1}{j^{3/2}} \exp \left[j\beta \left(\mu - \sum_{i=1}^3 \frac{mx_i^2 \omega_i^2}{2(1 + \omega_i^2 t^2)} \right) \right] dz \\
&= \kappa \sum_{j=1}^{\infty} \frac{1}{j^{3/2}} \int_{-\infty}^{\infty} \exp \left[-\frac{j m \omega_z^2 z^2}{2k_B T (1 + \omega_z^2 t^2)} \right] dz \cdot \exp \left[\frac{\mu}{k_B T} - \frac{m}{2k_B T} \sum_{i=1}^2 \frac{\omega_x^2 x_i^2}{1 + \omega_i^2 t^2} \right] \\
&= \kappa \sum_{j=1}^{\infty} \frac{1}{j^{3/2}} \int_{-\infty}^{\infty} \exp [-j\varpi z^2] dz \cdot \varsigma^j
\end{aligned} \tag{4.12}$$

where I have defined

$$\varsigma = \exp \left[\frac{\mu}{k_B T} - \frac{m}{2k_B T} \sum_{i=1}^2 \frac{\omega_x^2 x_i^2}{1 + \omega_i^2 t^2} \right]$$

and

$$\varpi = \frac{m \omega_z^2}{2k_B T (1 + \omega_z^2 t^2)}.$$

So the 2D integrated profile of a thermal atom cloud is:

$$\begin{aligned}
n_{th}(x, y, t) &= \kappa \sum_{j=1}^{\infty} \frac{1}{j^{3/2}} \sqrt{\frac{\pi}{j\varpi}} \cdot \varsigma^j \\
&= \frac{\kappa}{\sqrt{\varpi}} \sum_{j=1}^{\infty} \frac{\varsigma^j}{j^2} \\
&= \frac{\kappa}{\sqrt{\varpi}} \text{Li}_2(\varsigma),
\end{aligned}$$

which is in full

$$\begin{aligned}
n_{th}(x, y, t) &= \frac{1}{\sqrt{1 + \omega_x^2 t^2} \sqrt{1 + \omega_y^2 t^2}} \frac{\hbar}{\lambda_T^4 m \omega_z} \text{Li}_2(\varsigma) \\
&= \frac{1}{2\pi \sqrt{1 + \omega_x^2 t^2} \sqrt{1 + \omega_y^2 t^2}} \left(\frac{a_z}{\lambda_T^2} \right)^2 \text{Li}_2(\varsigma),
\end{aligned} \tag{4.13}$$

where $a_z = \sqrt{\frac{\hbar}{m \omega_z}}$ is the harmonic oscillator length in the z direction.

4.3.3.3 Derivation of the Density of the Condensate

The macroscopic state of the condensate is well described by the Gross-Pitaevski Equation [39]

$$i\hbar \frac{\partial}{\partial t} \Psi(\mathbf{r}, t) = \left(-\frac{\hbar^2 \nabla^2}{2m} + V_{ext}(\mathbf{r}) + U_{int} |\Psi(\mathbf{r}, t)|^2 \right) \Psi(\mathbf{r}, t) \quad (4.14)$$

where $V_{ext}(\mathbf{r})$ is the external potential the particles are in, (usually a harmonic trap) and $U_{int} |\Psi(\mathbf{r}, t)|^2$ represents the interaction energy, i.e. the energy required to have a density of $|\Psi(\mathbf{r}, t)|^2$ particles close enough together, where $U_{int} = \frac{4\pi\hbar^2 a}{m}$ is the coupling constant and a is the s -wave scattering length of ^{87}Rb . In this mean field- approximation, $\Psi(\mathbf{r}, t)$ is the mean-field i.e. the expectation of an annihilation operator at a given position and time;

$$\begin{aligned} \Psi(\mathbf{r}, t) &= \langle \hat{\psi}(\mathbf{r}, t) \rangle \\ &= \left\langle \delta(\mathbf{r} - \mathbf{r}', t - t') \sum_i c_i \hat{a}_i \right\rangle, \end{aligned}$$

where \hat{a}_i annihilates a single particle in the energy eigenstate ε_i . The time independent GP equation is [50]

$$\mu \Psi(\mathbf{r}, t) = \left(-\frac{\hbar^2 \nabla^2}{2m} + V_{ext}(\mathbf{r}) + U_{int} |\Psi(\mathbf{r}, t)|^2 \right) \Psi(\mathbf{r}, t) \quad (4.15)$$

where the eigenvalue is not the usual energy per particle E , but instead we have $i\hbar \frac{\partial}{\partial t} \Psi \rightarrow \mu \Psi$ where μ is the chemical potential. In the non-interacting case $U_{int} = 0$ and $\mu = E$, but in the interacting case since $U_{int} \neq 0$ we have $\mu \neq E$ [50].

In the Ideal Gas limit, the particles are non-interacting, and thus $U_{int} = 0$. Then equation (4.14) becomes

$$i\hbar \frac{\partial}{\partial t} \Psi(\mathbf{r}, t) = \left(-\frac{\hbar^2 \nabla^2}{2m} + V_{ext}(\mathbf{r}) \right) \Psi(\mathbf{r}, t)$$

which is just N independent one-particle Schrödinger equations. Thus the condensate shape will be simply the shape of the ground state energy eigenfunction of the trap. In the harmonic case $V_{ext}(\mathbf{r}) = m(\omega_x^2 x^2 + \omega_y^2 y^2 + \omega_z^2 z^2)$, the equation is separable, and the harmonic oscillator solutions are given by

$$\begin{aligned} \psi_{n_x n_y n_z}(\mathbf{r}) &= \left(\frac{m\bar{\omega}}{\pi\hbar} \right)^{3/4} \prod_{i=1,2,3} \frac{H_{n_i}(\xi_i)}{\sqrt{2^{n_i} n_i!}} e^{-\xi_i^2/2} \\ E_{n_x n_y n_z} &= \hbar\omega_x \left(n_x + \frac{1}{2} \right) + \hbar\omega_y \left(n_y + \frac{1}{2} \right) + \hbar\omega_z \left(n_z + \frac{1}{2} \right) \end{aligned}$$

where $\xi_i = \sqrt{\frac{m\omega_i}{\hbar}} x_i$ is the normalized H.O. coordinate, $\bar{\omega} = \sqrt[3]{\omega_x \omega_y \omega_z}$ is the geometric mean of the trapping frequencies, and $H_n(x)$ is the n th Hermite polynomial.

So the BEC has the shape of a gaussian in this limit, as

$$\begin{aligned} |\psi_{000}(\mathbf{r})|^2 &= \left(\frac{m\bar{\omega}}{\pi\hbar} \right)^{3/2} \prod_{i=1,2,3} e^{-\xi_i^2} \\ &= \left(\frac{m\bar{\omega}}{\pi\hbar} \right)^{3/2} e^{-\frac{m}{\hbar}(\omega_x x^2 + \omega_y y^2 + \omega_z z^2)} \end{aligned}$$

so that

$$\begin{aligned} |\Psi_c(\mathbf{r})|^2 &= N_c |\psi_{000}(\mathbf{r})|^2 \\ &= N_c \left(\frac{m\bar{\omega}}{\pi\hbar} \right)^{3/2} e^{-\frac{m}{\hbar}(\omega_x x^2 + \omega_y y^2 + \omega_z z^2)}. \end{aligned} \quad (4.16)$$

Now when the trap is turned off, the wavefunction evolves from the state above as a free particle when considered in the centre-of-mass frame (which will fall under gravity),

$$i\hbar \frac{\partial}{\partial t} \Psi(\mathbf{r}, t) = -\frac{\hbar^2 \nabla^2}{2m} \Psi(\mathbf{r}, t)$$

so $\Psi_c(\mathbf{r}, t)$ is given in the usual fashion [51] by

$$\begin{aligned} \Psi_c(\mathbf{r}, t) &= \frac{1}{(2\pi)^3} \iiint \iiint \Psi_c(\mathbf{r}_0, 0) e^{-i\mathbf{k}\cdot\mathbf{r}_0} d^3\mathbf{r}_0 e^{i(\mathbf{k}\cdot\mathbf{r} - \frac{\hbar k^2}{2m}t)} d^3\mathbf{k} \\ &= \frac{\sqrt{N_c} \left(\frac{m\bar{\omega}}{\pi\hbar} \right)^{3/4}}{(2\pi)^3} \iiint \iiint e^{-\frac{m}{2\hbar}(\omega_x x_0^2 + \omega_y y_0^2 + \omega_z z_0^2)} e^{-i\mathbf{k}\cdot\mathbf{r}_0} d^3\mathbf{r} e^{i(\mathbf{k}\cdot\mathbf{r} - \frac{\hbar k^2}{2m}t)} d^3\mathbf{k} \\ &= \frac{\sqrt{N_c} \left(\frac{m\bar{\omega}}{\pi\hbar} \right)^{3/4}}{(2\pi)^3} \left(\frac{m\bar{\omega}}{2\pi\hbar} \right)^{-3/2} \iiint \left(\prod_{j=1}^3 e^{-\frac{\hbar k_j^2}{2m\omega_j}} \right) e^{i(\mathbf{k}\cdot\mathbf{r} - \frac{\hbar k^2}{2m}t)} d^3\mathbf{k} \\ &= \frac{\sqrt{N_c} \left(\frac{m\bar{\omega}}{\pi\hbar} \right)^{-3/4}}{(\sqrt{2}\pi)^3} \prod_{j=1}^3 \int e^{-\frac{\hbar k_j^2}{2m} \left(\frac{1}{\omega_j} + it \right) + ik_j x_j} dk_j \\ &= \frac{\sqrt{N_c} \left(\frac{m\bar{\omega}}{\pi\hbar} \right)^{-3/4}}{(\sqrt{2}\pi)^3} \prod_{j=1}^3 \sqrt{\frac{2m\omega_j \pi}{\hbar(1+i\omega_j t)}} e^{-\frac{m\omega_j x_j^2}{2\hbar(1+i\omega_j t)}} \\ &= \sqrt{N_c} \left(\frac{m\bar{\omega}}{\pi\hbar} \right)^{3/4} \prod_{j=1}^3 \sqrt{\frac{1-i\omega_j t}{1+\omega_j^2 t^2}} e^{-\frac{m\omega_j x_j^2(1-i\omega_j t)}{2\hbar(1+\omega_j^2 t^2)}} \end{aligned}$$

and finally, the density is given by

$$\begin{aligned} |\Psi_c(\mathbf{r}, t)|^2 &= N_c \left(\frac{m\bar{\omega}}{\pi\hbar} \right)^{3/2} \prod_{j=1}^3 \frac{2m\omega_j \pi}{\hbar \sqrt{1+\omega_j^2 t^2}} e^{-\frac{m\omega_j x_j^2}{\hbar(1+\omega_j^2 t^2)}} \\ &= N_c \left(\frac{m\bar{\omega}}{\pi\hbar} \right)^{3/2} \prod_{j=1}^3 \frac{1}{\sqrt{1+\omega_j^2 t^2}} e^{-\frac{m\omega_j x_j^2}{\hbar(1+\omega_j^2 t^2)}} \end{aligned} \quad (4.17)$$

which is still a Gaussian. This is a good approximation for small atom numbers, where the interaction term U_{int} will play less of a role. For the case of a large number of atoms in the ground state, the Thomas-Fermi approximation is better.

In the Thomas-Fermi approximation it is assumed that since the kinetic energy in the ground state is minimal, we may as well ignore it altogether at $T = 0$. This means that $-\frac{\hbar^2 \nabla^2}{\Psi(\mathbf{r}, t) 2m} \Psi(\mathbf{r}, t) \ll V_{ext}(\mathbf{r}), U_{int} |\Psi(\mathbf{r}, t)|^2$ and equation (4.14) becomes (in the time-

independent case)

$$\begin{aligned}\mu\Psi(\mathbf{r}) &= \left(V_{ext}(\mathbf{r}) + U_{int}|\Psi(\mathbf{r})|^2\right)\Psi(\mathbf{r}) \\ \mu &= V_{ext}(\mathbf{r}) + U_{int}|\Psi(\mathbf{r})|^2 \\ |\Psi(\mathbf{r})|^2 &= \begin{cases} \frac{\mu - V_{ext}(\mathbf{r})}{U_{int}} & \mu \geq V_{ext}(\mathbf{r}) \\ 0 & \mu < V_{ext}(\mathbf{r}) \end{cases}\end{aligned}\quad (4.18)$$

which in the case of a harmonic potential $V_{ext}(\mathbf{r}) = \frac{m}{2}(\omega_x^2x^2 + \omega_y^2y^2 + \omega_z^2z^2)$ gives the BEC a paraboloid density function. At the edges of the function where $\mu = V_{ext}(\mathbf{r})$, the second derivative diverges to infinity and the interaction energy is zero so the assumption $-\frac{\hbar^2\nabla^2}{\Psi(\mathbf{r},t)2m}\Psi(\mathbf{r},t) \ll U_{int}|\Psi(\mathbf{r},t)|^2$ breaks down. Thus the edges will be ‘rounded off’ a little by the kinetic energy contribution here. Equation (4.18) becomes exact in the limit $T = 0, N \rightarrow \infty$ [50]. It can be shown that this macroscopic wave function will evolve to a rescaled paraboloid under ballistic expansion [39, 40].

4.3.3.4 Calculation of the Optical Thickness of the Condensate Fraction

To find the column density of the BEC for comparison with imaging we must integrate along the imaging axis z .

$$n_c(x, y, t) = \int_{-\infty}^{\infty} \rho_c(\mathbf{r}, t) dz \quad (4.19)$$

In the ideal gas limit the density of the condensate is given by equation (4.17). Thus

$$\begin{aligned}n_{c\text{ideal}}(x, y, t) &= \int_{-\infty}^{\infty} \rho_{c\text{ideal}}(\mathbf{r}, t) dz \\ &= N_c \left(\frac{m\bar{\omega}}{\pi\hbar}\right)^{3/2} \int_{-\infty}^{\infty} \prod_{j=1}^3 \frac{1}{\sqrt{1+\omega_j^2 t^2}} e^{-\frac{m\omega_j x_j^2}{\hbar(1+\omega_j^2 t^2)}} dz \\ &= N_c \left(\frac{m}{\pi\hbar}\right)^2 \omega_z \prod_{j=1}^2 \frac{\omega_j}{\sqrt{1+\omega_j^2 t^2}} e^{-\frac{m\omega_j x_j^2}{\hbar(1+\omega_j^2 t^2)}}\end{aligned}$$

In the Thomas-Fermi limit the density of the condensate is paraboloidal, so

$$\begin{aligned}n_{c\text{TF}}(x, y, t) &= \int_{-\infty}^{\infty} \rho_{c\text{TF}}(\mathbf{r}, t) dz \\ &= \int_{\text{parabola}} A(t) - X(t)x^2 - Y(t)y^2 - Z(t)z^2 dz \\ &= A'(t) - X'(t)x^2 - Y'(t)y^2\end{aligned}\quad (4.20)$$

which is still paraboloidal. Thus we use a parabolic fit to the condensate in section 4.3.4.

4.3.3.5 Measurement of temperature

Approximating the polylogarithm function $\text{Li}_2(\zeta)$ by the first term in the sum (4.10) (see Figure 4.7), the thermal column density given by equation (4.13) becomes

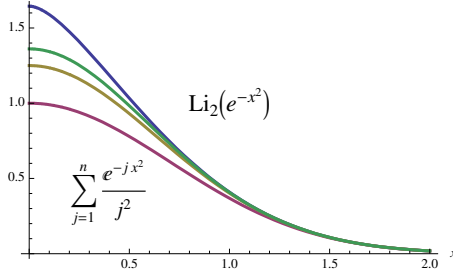


Figure 4.7: Comparison of $\text{Li}_2(e^{-x^2})$ (blue) with its first few terms $\sum_{j=1}^n e^{-jx^2}/j^2$ for $n = 1$ (red), 2 (yellow) and 3 (green). It can be seen that the first order gaussian term dominates in the wings, and so gives a reasonable approximation to find the temperature.

$$n_{th}(x, y, t) = \frac{\kappa}{\sqrt{\varpi}} \exp \left[\frac{\mu}{k_B T} - \frac{m}{2k_B T} \sum_{i=1}^2 \frac{\omega_i^2 x_i^2}{1 + \omega_i^2 t^2} \right]$$

where $n_0 = \kappa/\sqrt{\varpi}$. Assuming $\mu \approx 0$ for large total atom number N , the density reduces further to

$$n_{th}(x, y, t) = \frac{\kappa}{\sqrt{\varpi}} \exp \left[-\frac{x^2}{2\sigma_x^2} - \frac{y^2}{2\sigma_y^2} \right] \quad (4.21)$$

which is a gaussian with standard deviation in the i th direction given by

$$\sigma_i^2 = \left(\frac{1}{\omega_i^2} + t^2 \right) \frac{k_B T_i}{m}. \quad (4.22)$$

This suggests a simple method for estimating the temperature of a cloud of atoms by fitting a gaussian to the thermal portion. Equation (4.22) is conveniently of the form $y = mx + c$ (where $y = \sigma_i^2$, $x = t^2$) and thus the gradient of this equation is related to the temperature by the factor k_B/m . Finding the temperature of an atom cloud by this method involves taking several pictures of the same cloud at different expansion times, and is illustrated on the left of Figure 4.8. To use this method to fit a bimodal cloud, a bimodal fit must be used. We use a parabolic fit to the BEC fraction as per (4.18) with a Gaussian fit to the thermal fraction as per equation (4.21), both fit over the entire cloud.

A quicker method for finding the temperature of the cloud is to take a single absorption image and use the trap frequencies ω_r and ω_a to calculate the temperature directly via equation (4.22). This is illustrated on the right of Figure 4.8, where it is compared to the previous method. The one-shot method has the advantage that more measurements can be made before long-duration fluctuations (over about 30 minutes or so) can affect the BEC machine, thus it is this method that is used for number calibration in the next section.

4.3.4 Number calibration

4.3.4.1 Derivation of condensate fraction

In the thermodynamic limit $N \rightarrow \infty, \mu \rightarrow 0$, the number of atoms in the thermal cloud $N_{th} = N - N_0$ can be obtained by integrating equation (4.9) over all space

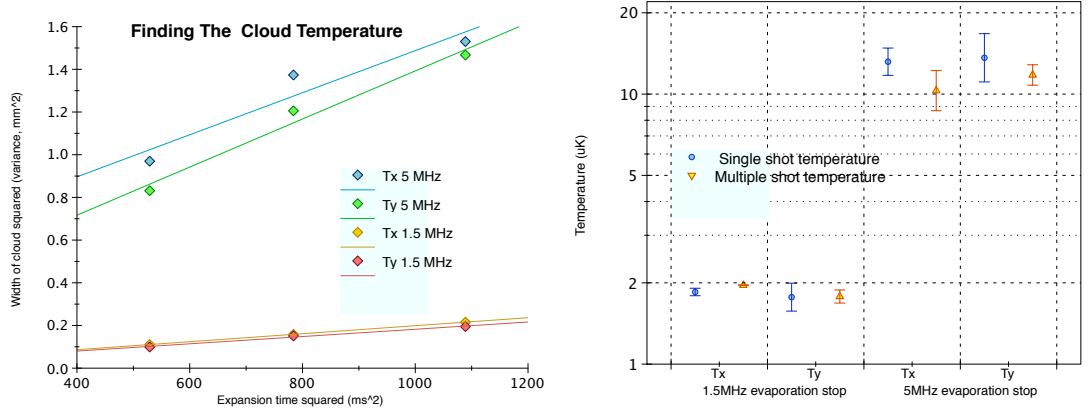


Figure 4.8: Two methods were compared for finding the temperature of the thermal portion of the cloud. **Left:** Temperature measurement by the gradient method from multiple absorption images, using equation (4.22). The upper (lower) two lines find the temperature from the standard deviation width in the x and y directions of a cloud where evaporation was stopped at 5MHz (1.5MHz) . **Right:** The temperature as calculated by the gradient method (orange triangles, equation (4.22)) is compared to the temperature as calculated from a single absorption image and the trap frequencies as measured in section 4.3.2 (blue circles). Theoretically, $T_x = T_y = T$ for a single cloud and this data conforms within its uncertainties.

$$\begin{aligned}
 N - N_0 &= \iiint \rho_{th}(\mathbf{r}, t) d^3\mathbf{r} \\
 &= \iiint \left(\prod_{i=1}^3 \frac{1}{\sqrt{1 + \omega_i^2 t^2}} \right) \frac{1}{\lambda_T^3} \text{Li}_{3/2}(\vartheta) d^3\mathbf{r} \\
 &= \left(\prod_{i=1}^3 \frac{1}{\sqrt{1 + \omega_i^2 t^2}} \right) \frac{1}{\lambda_T^3} \sum_{j=1}^{\infty} \iiint \frac{\vartheta^j}{j^{3/2}} d^3\mathbf{r} \\
 &= \left(\prod_{i=1}^3 \frac{1}{\sqrt{1 + \omega_i^2 t^2}} \right) \frac{1}{\lambda_T^3} \sum_{j=1}^{\infty} \frac{1}{j^{3/2}} \iiint \exp \left(j\beta \left(\sum_{i=1}^3 \frac{m \omega_i^2 t^2}{2(1 + \omega_i^2 t^2)} \right) \right) d^3\mathbf{r} \\
 &= \left(\frac{\sqrt{2\pi k_B T}}{\bar{\omega} \lambda_T \sqrt{m}} \right)^3 \sum_{j=1}^{\infty} \frac{1}{j^3} \\
 &= \left(\frac{k_B T}{\bar{\omega} \hbar} \right)^3 \zeta(3)
 \end{aligned}$$

where $\zeta(z) = \sum_{j=1}^{\infty} 1/j^z$ is the Riemann zeta function. Dividing through by N gives the equation

$$\frac{N_0}{N} = 1 - \left(\frac{T}{T_0} \right)^3 \quad (4.23)$$

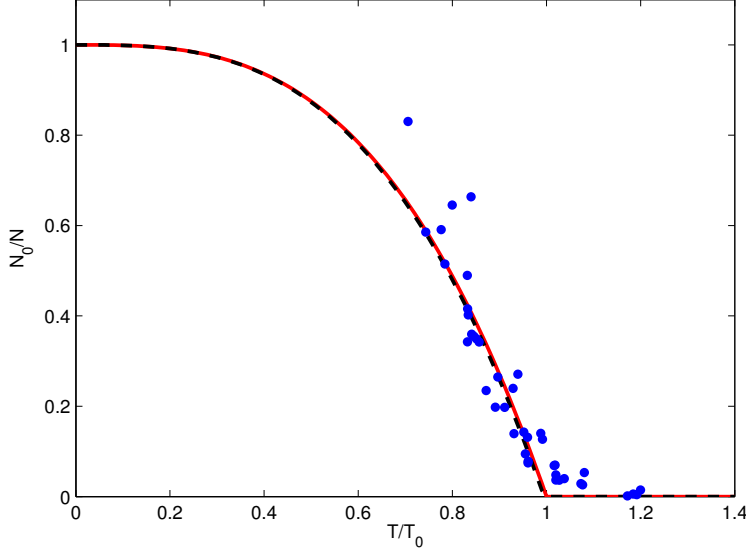


Figure 4.9: Fraction of atoms in the ground state N_0/N against temperature T rescaled to the critical temperature in the thermodynamic limit $T_0 = \frac{\hbar\omega}{k_B} \sqrt[3]{\frac{N}{\zeta(3)}}$. The red line is the thermodynamic prediction for $N \rightarrow \infty$, i.e. equation (4.23). The black dashed line is a line of best fit of the form $N_0/N = 1 - (T/\alpha T_0)^3$ which gives the intercept as $\alpha = 0.995 \pm 0.007$. For a number of approximately 3×10^5 atoms at transition, a finite-number correction (4.25) to the thermodynamic limit gives $\alpha = T_0^{finite}/T_0 = 0.989$.

where I have defined T_0 as the function of N given by

$$T_0 = \frac{\hbar\omega}{k_B} \sqrt[3]{\frac{N}{\zeta(3)}}. \quad (4.24)$$

An accurate finite number correction $N \rightarrow \infty$ has been derived by Ketterle and van Druten [52] which gives

$$T_0^{finite} = \frac{\hbar\omega}{k_B} \left(\sqrt[3]{\frac{N}{\zeta(3)}} - \frac{\pi^2}{12\zeta(3)} \right). \quad (4.25)$$

4.3.4.2 Measurement of condensate fraction

In our measurement of the critical temperature shown in Figure 4.9, we had approximately 3×10^5 atoms at transition, which makes $T_0 = 243$ nK and the finite-number correction $T_0^{finite} = 0.989 \times T_0 = 242$ nK.

To measure the fraction of atoms in the ground state N_0/N , a bimodal fit was performed over the whole cloud, and the width of the thermal gaussian was used to determine the temperature T as in the previous section. Our experimental result follows the predicted curve (4.23) nicely, so it compares favourably with the literature⁸ [4]. The smooth bend (as opposed to the sharp corner of equation (4.23)) in the data around $T/T_0 \approx 1$ is probably due to our fitting method, which will tend to overestimate the condensate fraction in this region. This is because of the extra density in the Bose-enhanced distribution around the

⁸And even more favourably [53] against some.

centre of the cloud (as compared to our gaussian fit , see Figure 4.7) will be fit instead by the parabola we have designed to fit the condensate fraction.

4.3.4.3 Calibration of atom number

To calibrate our atom number with this data, use (4.23)

$$T_0 = \frac{\hbar\bar{\omega}}{k_B} \sqrt[3]{\frac{N}{\zeta(3)}}$$

and rearrange for N ,

$$N = \zeta(3) \left(\frac{k_B T_0}{\hbar\bar{\omega}} \right)^3.$$

So now

$$\Delta N = 3\zeta(3) \left(\frac{k_B T_0}{\hbar\bar{\omega}} \right)^2 \sqrt{\left(\frac{k_B \Delta T_0}{\hbar\bar{\omega}} \right)^2 + \left(\frac{k_B T_0 \Delta \bar{\omega}}{\hbar\bar{\omega}^2} \right)^2}$$

and

$$\begin{aligned} \frac{\Delta N}{N} &= 3 \cdot \sqrt{\left(\frac{\Delta T_0}{T_0} \right)^2 + \left(\frac{\Delta \bar{\omega}}{\bar{\omega}} \right)^2} \\ &= 3 \cdot \sqrt{\left(\frac{0.007}{0.995} \right)^2 + 2 \left(\frac{0.3}{209.2} \right)^2 + \left(\frac{0.1}{19.4} \right)^2} \\ &= 0.027. \end{aligned}$$

So we have an uncertainty in our absolute atom number measurements of 2.7%.

4.4 What should it look like?

A useful thing to do at this stage is to simulate our data numerically so we know what to expect. For the purposes of the simulation, the simple absorption model of sections 3.2.1 and 3.4.2 was implemented. A realistic number (10^5) of atoms was distributed with a gaussian shape, over a pixelated ‘image’, $n(x, y)$. Then, atom shot noise was added to the image by adding a random poissonian-distributed deviation from each pixel’s previous value. This is shown in Figure 4.10. Photon shot noise was also included, by creating a background image $m_0(x, y)$ which had poissonian variation in electron count, around a mean of $10,000 e^-$ (which was chosen as a value for a reasonably full electron well, without inducing saturation of the CCD array, c.f. section 4.2.1). Then, the second image $m_f(x, y)$ had the atom cloud’s shadow imparted upon it by equation(3.3),

$$m_f(x, y) = \langle m_0(x, y) \rangle e^{-n(x, y)\sigma},$$

followed by the addition of poissonian photon shot noise to each pixel in $m_f(x, y)$. A final step in preparing the data is to blur the images $m_0(x, y)$ and $m_f(x, y)$ (c.f. section 3.5) by applying a filter which replaces each pixel by a weighted average of itself and its nearest neighbours, as in equation (3.22). Once the images have been generated, the atom

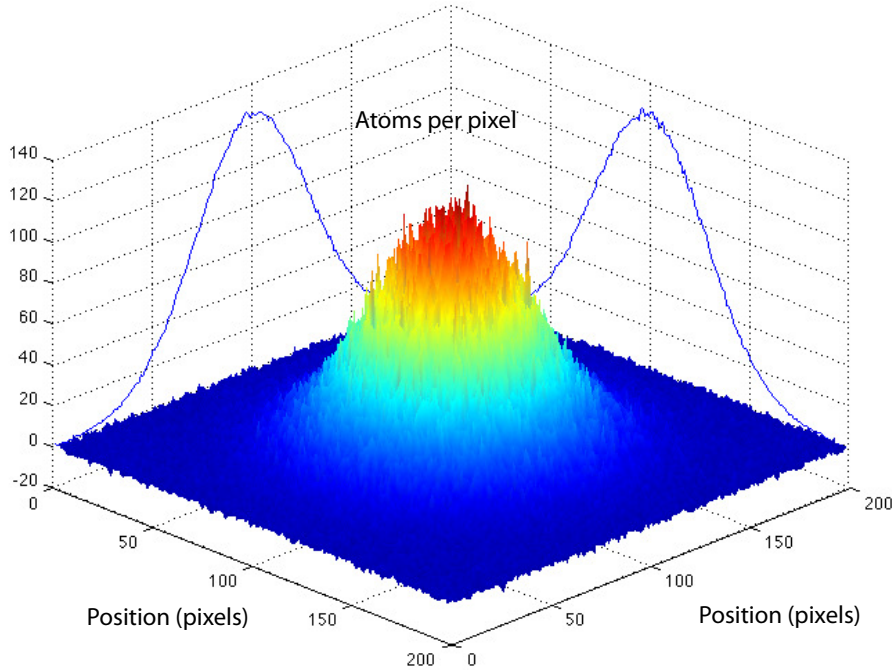


Figure 4.10: The theoretically computed atom density image, with no blurring applied. Height indicates the number of atoms per pixel. The projections are the integrated cross-sections of the image, normalised to be the same height as the cloud.

distribution is again calculated by equation (3.4),

$$n'(x, y) = \frac{1}{\sigma} \ln \left(\frac{I_0(x, y)}{I_f(x, y)} \right)$$

Through this method, the atom distribution calculated will have the appropriate noise statistics and blurring as it would in real experimental data. An image generated by this method is shown in Figure 4.11, along with its noise as calculated by the nearby averaging procedure (see section A.3). It is important to note the striking difference between the atomic shot noise as seen without any blurring processes, and as seen with blurring. It is the latter which we will see in the experiments due to the numerous effects described in section 3.5, which will *decrease* the noise observed from the expected level when measured pixel by pixel⁹. To observe atomic shot noise on these blurry images, we must bin the pixels together to form larger $N \times N$ pixel bins. This effectively reduces the fraction of the pixel length blurred across from ϵ to ϵ/N^2 . The effectiveness of this method can be seen on the right of Figure 4.11.

⁹However, the noise is still there and still reduces the sensitivity of our atom number counting. The blurring simply violates the assumption that each pixel is an independent sample from the atom and photon distributions, because the measured values of each pixel are correlated by equation (3.22).

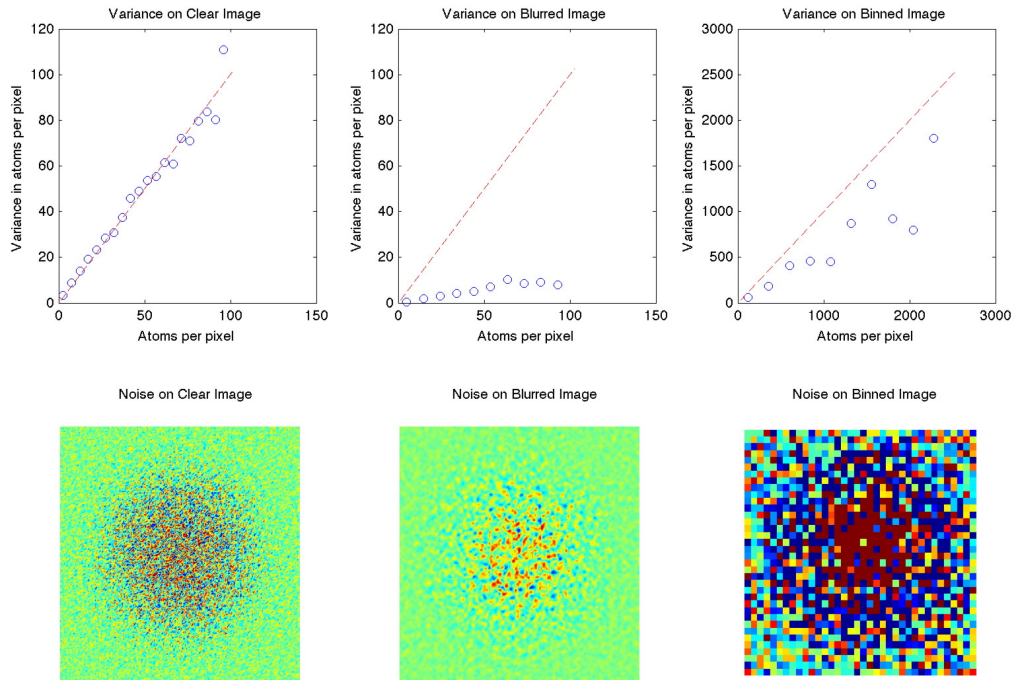


Figure 4.11: Numerical data computed to have the statistical properties of blurred atomic shot noise on an atom cloud of 5×10^5 atoms. **Left, Bottom:** The difference from the nearby average on the theoretical atom cloud with no blurring. **Left, Top:** The atomic shot noise variance as calculated from the noise image below. **Center, Bottom:** The difference from the nearby average on the theoretical atom cloud after blurring by $\epsilon = 0.5$ pixels. **Center, Top:** It is seen that blurring severely impacts our ability to see the atomic shot noise variance in the raw image. This data is consistent with previous attempts to see shot noise, such as [19]. **Right, Bottom:** The difference from the nearby average on the theoretical atom cloud after blurring by $\epsilon = 0.5$ pixels, but then binned into 5×5 pixel bins. **Right, Top:** The atom shot noise becomes visible once more after binning into 5×5 pixel bins, as this effectively reduces the fraction of a pixel blurred across to $\epsilon/N^2 = 0.5/25 = 0.02$.

Observation of Atomic Shot Noise

Let us analyse an experimental image of a small thermal cloud, with the aim of comparing it to the numerical data of the previous chapter. The cloud has a temperature of 510nK, and a total of 2.5×10^5 atoms, and its standard deviation widths σ_i in the horizontal and vertical directions are $72\mu\text{m}$ and $38\mu\text{m}$ respectively. The average number of electrons in the background image is $\langle m \rangle = 10,400$; which is almost the full well depth of the CCD array, without saturating the image. Thus, this cloud is the perfect candidate to compare to the predictive data in Figure 4.11. The experimental analysis is shown in Figures 5.1 and 5.3. Figure 5.1 shows that our data is in fact blurred slightly, and so the variance only shows half of the atom shot noise. As such, we see only part of the atomic shot noise on this image. An analysis of the sources of blur as per section 3.5 shows the following breakdown of the blurring: thermal blurring = $0.3\mu\text{m}$, gravity blurring = $0.8\mu\text{m}$ (only in the vertical direction), photon recoil blurring = $0.6\mu\text{m}$ (with $\Delta = 6.1\text{ MHz}$, $I/I_{\text{sat}} \approx 3$), diffraction limit of optics = $1.9\mu\text{m}$. It would seem from this data that the main source of blurring is the diffraction limit of our imaging system. Even though the data in Figure 5.1 shows half the expected atom shot noise, it is still more than twice as good as the data in [19], which achieved only a factor of 0.17 of atomic shot noise.

To overcome this blurring effect, we bin the pixels together, effectively reducing the fraction of a pixel length blurred across, ϵ . The same atom cloud image is analysed in Figure 5.2, but this time it has been binned into 2×2 pixels before analysis. Here it can be seen that the variance on each binned pixel agrees quantitatively with the theoretical result for atom + photon shot noise, as predicted by the theory (see the right of Figure 4.11). For larger bin sizes, the noise stays on this limit until the the bin size gets so large that the approximation (3.5) is invalid, the nearby averaging procedure envelops the entire cloud, or the assumption that we are sampling a small fraction of the cloud (inherent in equation (3.11)) is incorrect. This shows that classical noise is not the source of the variance, because if it were, the noise would increase beyond the atomic noise limit with further binning. Figures 5.1 and 5.2 show the measured photon shot noise as slightly higher than the predicted value (photon shot noise can be found as the intercept in the variance graphs).

It is interesting to compare these results to the situation where the detuning Δ from the resonant imaging frequency is small. Figure 5.3 shows the analysis of a similar atomic cloud, this time imaged with 2 MHz detuning from the resonant imaging frequency (as opposed to 6.1 MHz in the previous figures). It is fairly clear from Figure 5.3 (b) that the blurring has increased, and the atomic shot noise is now unresolvable from the photon shot noise. As all the parameters of the experiment are the same except for the detuning Δ , the only contribution to the blurring which has changed is the random walk due to photon recoil. This has changed because at smaller detunings, the atoms have a higher

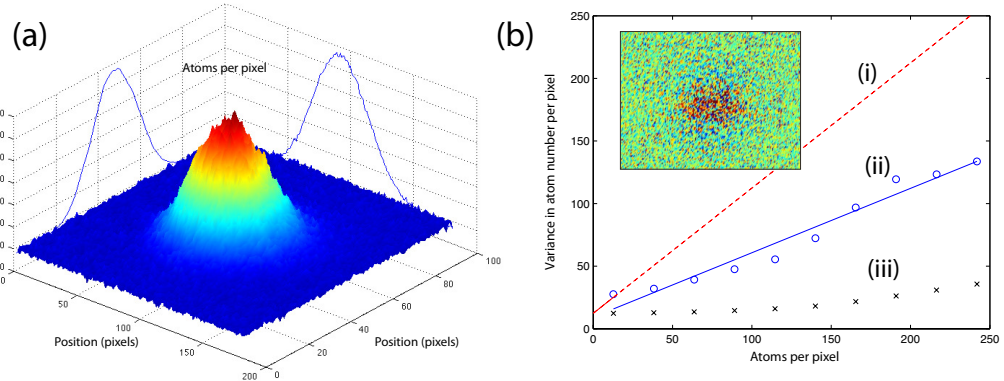


Figure 5.1: Experimental data from a small atomic cloud, with no binning. (a) The atomic density image. The height on the image indicates the number of atoms at each pixel. The image is $360\mu\text{m}$ wide and $210\mu\text{m}$ high at the atom cloud, and was taken after a 5.7ms ballistic expansion, with a $30\mu\text{s}$ imaging pulse which was detuned 6.1 MHz from the atomic resonance. The cloud has a temperature of 510nK , and a total of 2.5×10^5 atoms. The projections are the integrated cross-sections of the image, normalised to be the same height as the cloud. (b) The theoretical photon shot noise is shown in black ($\text{x}'s$, (iii)) and the theoretical atomic shot noise (with photon shot noise) is shown in red (dashed, (i)). The blue points (ii) are experimental measurements of the variance of the image in (a) on the left, and are below atom shot noise due to blurring effects. The blue line is a line of best fit to the experimental data points. (b) **Inset:** Difference of the image in (a) from each pixel's nearby average (see appendix A.3), used to calculate the variance for each mean atom number on the left. Compare this image with the theoretical one in the centre bottom of Figure 4.11.

scattering rate and so the random walk spreads them further. The new estimate of the distance blurred due to photon recoil from equation (3.27) is $1.1\mu\text{m}$, now larger than all the other contributions other than the diffraction limit. Numerical simulations confirm that this increase in blurring is large enough to wash out the atomic shot-noise.

Binning the data improves the situation slightly, but not enough to get back near the theoretical atomic shot noise. It is interesting that this change in blurring due to photon recoil is the discriminating factor between data in which we can see atomic shot noise and that in which we cannot.

The important point is that Figure 5.2 shows that it is in fact clearly possible to observe the poissonian atomic shot noise, well and above the photon shot noise. It is encouraging to see such a large margin between the two, because this allows for the possibility of detecting sub-poissonian quantum noise on a Bose Einstein condensate. The only restriction now is that we need a BEC large enough to be able to bin our pixels together and see what its atomic quantum noise looks like, since at present our BECs are too small to achieve quantum noise visibility by this technique. Another way to approach absorption imaging of shot noise on a BEC is to improve the diffraction limit of the imaging system, as this is a major contribution to blurring of the image (see section 3.5). This would be achieved by using a shorter focal length lens, closer to the atom cloud. Increasing the magnification of the imaging system will not help yet, as our spatial resolution is now limited by blurring.

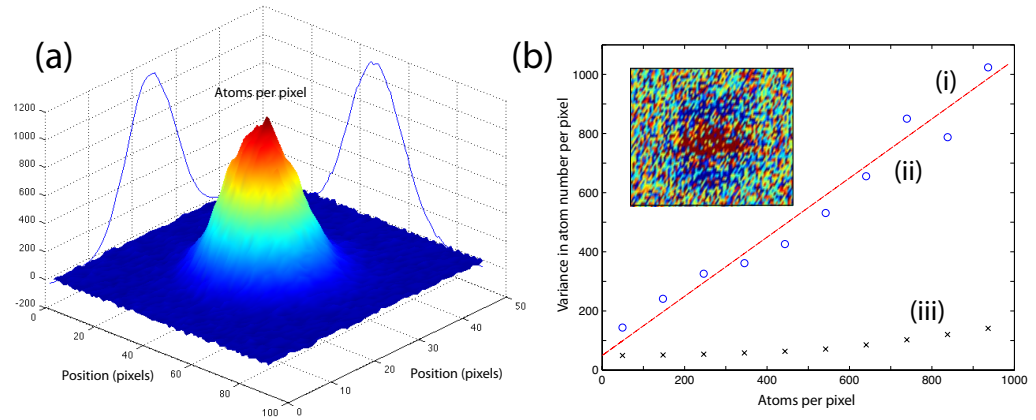


Figure 5.2: Experimental data from the same small atomic cloud shown in Figure 5.1, with 2×2 pixel binning to overcome the blurring effects. (a) The atomic density image. The height on the image indicates the number of atoms at each pixel. The image is $360 \mu\text{m}$ wide and $210 \mu\text{m}$ high at the atom cloud, and was taken after a 5.7 ms ballistic expansion, with a $30 \mu\text{s}$ imaging pulse which was detuned 6.1 MHz from the atomic resonance. The cloud has a temperature of 510 nK , and a total of 2.5×10^5 atoms. The projections are the integrated cross-sections of the image, normalised to be the same height as the cloud. (b) The theoretical photon shot noise is shown in black ('x's, (iii)) and the theoretical atomic shot noise (with photon shot noise) is shown in red (dashed, (i)). The blue points (ii) are experimental measurements of the variance of the image in (a) on the left, and it is clear that atom shot noise has been recovered by the binning. (b) **Inset:** Difference of the image in (a) from each pixel's nearby average (see appendix A.3), used to calculate the variance for each mean atom number on the left. Compare this image with the theoretical one in the bottom right of Figure 4.11.

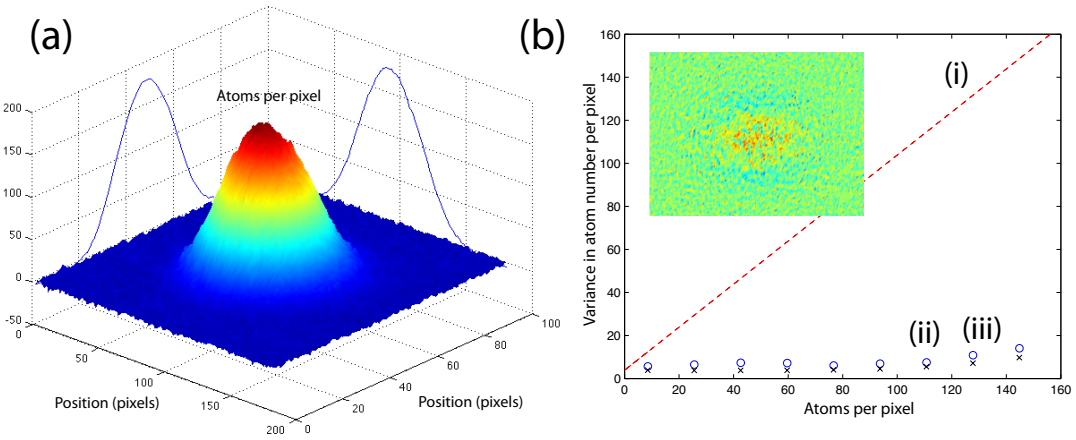


Figure 5.3: Experimental data from a similar cloud to the one in Figures 5.1 and 5.2, but this time imaged with near-resonant light. (a) The atomic density image. The height on the image indicates the number of atoms at each pixel. The image is 360 μm wide and 210 μm high at the atom cloud, and was taken after a 5.7 ms ballistic expansion, with a 30 μs imaging pulse which was detuned by 2 MHz from the atomic transition. The cloud has a temperature of 510 nK, and a total of 2.5×10^5 atoms. (b) The theoretical photon shot noise is shown in black (x's, (iii)) and the theoretical atomic shot noise (with photon shot noise) is shown in red (dashed, (i)). The blue points (ii) are experimental measurements of the variance of the image in (a) on the left, and evidently the atom shot noise has been washed out by the blurring, which is increased as compared with the blurring in the detuned image of Figure 5.1. (b) **Inset:** Difference of the image in (a) from each pixel's nearby average (see appendix A.3), used to calculate the variance for each mean atom number on the left. Compare this image with the theoretical one in the centre bottom of Figure 4.11.

Application to Atom Interferometry

Atom interferometers offer fundamental advantages over light interferometers in the field of precision measurement. The classic model presented in the introduction, showing that ten orders of magnitude in precision might be gained by using atoms in a Sagnac interferometer, is but one example of the increased precision atom interferometry offers [1]. In the days before BECs were realised, interferometers of matter-waves used thermal beams and micro-manufactured double slits or gratings [25]. Coherent atom interferometers from BECs are mostly constructed using either radio-frequency pulses [54] or sheets of light [55] as the diffraction gratings and beam splitters. These are much quicker and easier to construct and change during the course of an experiment, especially inside the vacuum chambers in which the cold-atom experiments take place. Interferometers built using coherent atom lasers (with a BEC as the source) have the possibility of using quantum mechanical squeezing to increase measurement precision, and this squeezing may be detectable by analysing the atomic noise on an absorption image. For almost all measurements up until now, thermal beams have been preferred since the reduction in noise by using coherent, squeezed sources must be balanced against the increase in signal gained by having a large number of atoms going through the device. However, as the size of BECs created gets larger, and as the noise on absorption images gets lower, atom lasers can potentially become the optimal choice. The other advantage cold atom interferometers have over thermal atomic beam interferometers is that they have a much narrower velocity spread. Since two-photon Raman interactions are highly velocity selective [37], beam splitters using this technique have a greater coherent transfer of the atom population using cold atom cloud sources. This is especially true where high-momentum-transfer beam splitters are used [56].

6.1 Our Atom Interferometer

Following the creation of a BEC as detailed in chapter 2, a pulse of coherent atoms from the BEC is out coupled from the trapped $|1, -1\rangle$ state to the untrapped $|1, 0\rangle$ state by a radio frequency pulse. The coherent atom pulse falls under gravity and passes through two ‘beam splitters’ which form the basis of the interferometer. These beam splitters are sheets of light which induce two-photon Raman transitions (see the original idea in [57] or a quick summary in [37]) between the $|1, 0\rangle$ and $|2, 0\rangle$ internal states (see Figure 6.1 (a)). After the atoms have passed through the interferometer, we detect how many are in each state. This is done by suddenly switching on the Ioffe trap for a short time to separate the clouds based upon their second-order Zeeman energy shifts, effecting a Stern-Gerlach experiment. Once the clouds in each state are separate, they are imaged as usual by

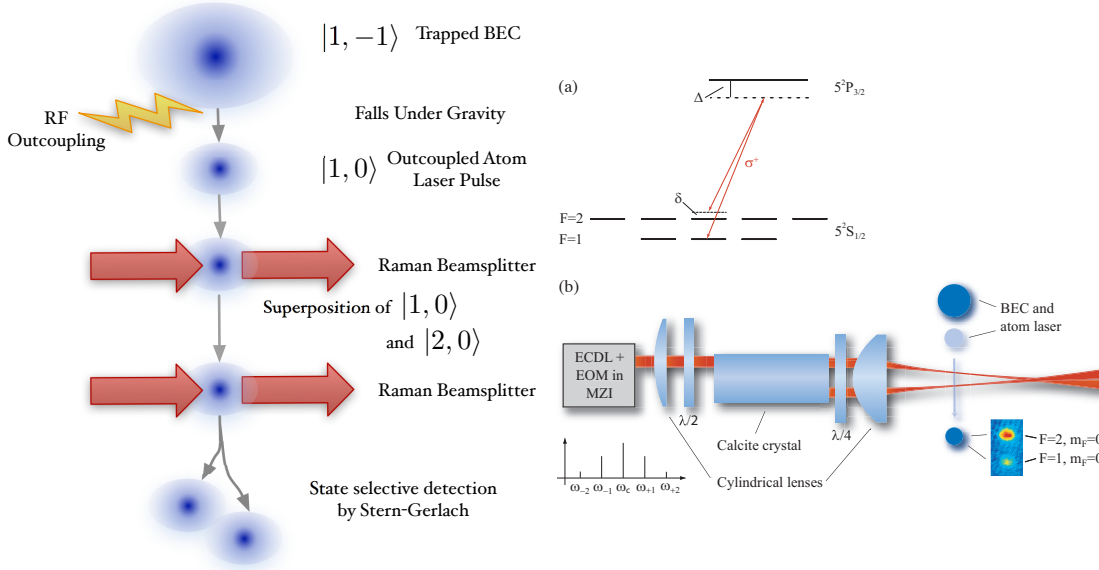


Figure 6.1: Scheme of atom interferometer. The notation $|F, m_F\rangle$ is used here. **Left:** A coherent atom cloud is out-coupled by a radio frequency pulse, which transfers some atoms in the BEC from the trapped $|1, -1\rangle$ state to the untrapped $|1, 0\rangle$ state. These atoms then fall under gravity and form the atom laser. In interaction region 2 some of them are transferred to the $|2, 0\rangle$ state by the Raman beam splitter. Atoms then evolve in the region between the beam splitters and develop a phase difference θ until interaction region 3, at which point the states are recombined by another Raman beam splitter. We then separate the the $|1, 0\rangle$ and $|2, 0\rangle$ internal states by the second-order Zeeman effect. How many atoms are in each state determines θ . **Right:** (a) Diagram illustrating the energetics of the two-photon Raman transition. Neither photon has sufficient energy to excite the transition between the $^{52}\text{S}_{1/2}$ and the $^{52}\text{P}_{3/2}$ fine structure levels, but together they can excite a two photon transition between the $|1, 0\rangle$ and $|2, 0\rangle$ atomic hyperfine $^{52}\text{S}_{1/2}$ levels. (b) Experimentally, the two sheets of light used for the interferometer are generated using the birefringence of a calcite crystal. The small difference in frequency between the two photons is realised by adding sidebands to a Raman laser beam with an electro-optic modulator.

absorption imaging¹. The relative atom number $(N_1 - N_2)/N$ relates to the phase difference acquired between the two states, and the result of many such experiments is shown in Figure 6.3, where the phase is adjusted via the two-photon detuning δ of the Raman light sheets. The resulting interference fringes are known as Ramsey fringes, because Ramsey was the first to try using two interaction regions rather than one, to narrow the linewidth and thus improve the accuracy of the measurement [37].

The improvements made in our absorption imaging system throughout my thesis have made a marked impact² upon the Ramsey fringes measured on the left of Figure 6.3, as compared to how they were before [55]. The stability measurements on the right of Figure

¹The $|1, 0\rangle$ state must be optically pumped into the $|2, 2\rangle$ state before imaging, but the imaging light itself pumps the $|2, 0\rangle$ state into the $|2, 2\rangle$ state in a short enough time to be ignored.

²Along with a new method of separating the atom clouds by the second-order Zeeman effect. Previously a two-stage imaging technique was used which introduced more relative atom noise and a small systematic error into the measurement of the number of atoms in the $|1, 0\rangle$ state. For details on the old technique, see [55].

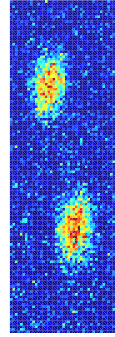


Figure 6.2: An example of the absorption images generated from the interferometer. The cloud on top is in the $|2, 0\rangle$ state and the one on the bottom is in the $|1, 0\rangle$ state.

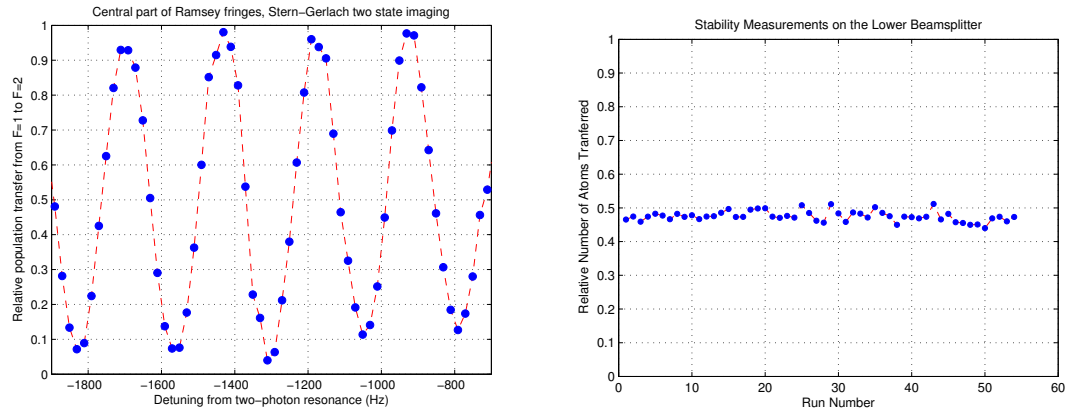


Figure 6.3: Left: Central portion of the Ramsey fringes taken with our atom interferometer. The detuning from two-photon resonance corresponds to δ in Figure 6.1 (a). **Right:** Stability measurements using one beam splitter. The data show a standard deviation over an hour's operation of $0.0155 = 1.5\%$ which is not quite at the atomic shot noise limit for a cloud of 5×10^3 atoms of $0.0071 = 0.7\%$. However there are other contributions to the noise apart from the imaging procedure.

6.3 show how the relative atom number varies over the course of an hour's operation with the detuning from two-photon resonance δ held at zero, only using the first beam splitter. In each run approximately 50% of the atoms have been transferred to the $|2, 0\rangle$ state³. In this way some sources of variation, such as a change in the distance between the beam splitters, are eliminated and so it is a better test of the noise introduced by the absorption imaging technique. The data show a standard deviation over an hour's operation of $0.0155 = 1.5\%$. The atomic shot noise limit for two clouds, each of 5×10^3

³This is known as a $\pi/2$ pulse in the terminology of the Bloch sphere, as it transfers the atoms from the $|1, 0\rangle$ state (which points down) to the $\frac{1}{\sqrt{2}}(|1, 0\rangle + e^{i\phi}|2, 0\rangle)$ state which rotates in the horizontal plane.

atoms, is given by

$$\begin{aligned}\Delta \left(\frac{N_2}{N_1 + N_2} \right) &= \frac{1}{2\sqrt{N}} \\ &= \frac{1}{2\sqrt{5 \times 10^3}} \\ &= 0.0071 \text{ or } 0.7\%\end{aligned}$$

So the images are not quite at the atomic shot noise limit. However there are other contributions to the noise apart from the imaging procedure, such as fluctuations in the intensity of the beam splitter, variation in the residual magnetic field after the trap is turned off, and fluctuations in the detuning from two-photon resonance. Once these other fluctuations are sorted out, it will be possible to tell whether the imaging system is atomic shot-noise limited. The eventual aim is that we can test various possibilities for squeezing the atom beam, thereby reducing the shot-to shot fluctuations and increasing the sensitivity of the interferometer as a precision measurement tool.

Conclusion and Outlook

*'A lightning flash:
between the forest trees
I have seen water.'*

Shiki, Masaoka. (1867-1902)

The results obtained in Chapter 5 clearly demonstrate that atomic shot noise has been quantitatively measured in cold atom clouds. As it is the dominant noise source in the regime where the detuning is large, we have achieved atomic shot-noise-limited imaging. The quantitative agreement with the theoretical model for atomic shot noise was achieved through binning of the data into larger pixels. This removes the effect of blurring, which is mainly caused by photon recoil and the diffraction limit of the imaging system. The binning method has been used before [8] to demonstrate atomic shot noise on a cold atom cloud. However, in that case much digital filtering was used to achieve clean images, in contrast to the results of this thesis. This imaging system will enable the investigation of the quantum statistics in a BEC, but limitations on the size of the BEC available and the diffraction-limited imaging system used have so far prevented this goal being achieved.

The atomic noise measurements made to obtain this result can conceivably be improved upon by several methods:

- Using a lens with a larger numerical aperture will improve the diffraction limit of our system. A larger numerical aperture is achieved with a larger diameter and a shorter focal length, but the focal length cannot be much less than 30mm due to the geometry of the setup and the magnification required to image the object onto a CCD. A good lens would be the achromatic doublet lens AC254-030-B from Thorlabs [58] which has a focal length of 30 mm and a diameter of 25.4 mm; it would roughly halve the size of the smallest detail we can resolve. An achromatic lens is chosen as these also reduce spherical aberration.
- Increasing the size of the condensates to be imaged. In our system, one way is to identify and eliminate the loss in transfer between the 3D MOT and the Ioffe coils, which reduces the atom number by a factor of 100. Another way is to slow down the radio frequency evaporation of the cloud. The limiting factor here is heat removal from the Ioffe trap, because if it operates continuously for longer than about 30 s, runaway resistive heating can damage the trap coils. A more drastic method for increasing the atom cloud size is to increase the size and power of the 3D MOT laser beams. Larger MOTs can also be achieved using the dark spot technique where no repump light illuminates the centre of the MOT [59]. This technique avoids re-absorption of scattered light from the cooling beam and therefore prevents some density-limiting and heating effects.
- Fitting the full density distribution functions derived in section 4.3 to the atom clouds to arrive at a ‘mean value’ for each pixel without resorting to the nearby

averaging procedure. The fitting routines used in sections 4.3.3.5 and 4.3.4 could also be improved by including higher order terms in the fit, however including too many more will make the routine slow to compute. Including the second and third order terms (depicted in Figure 4.7) would give a reasonable improvement in accuracy.

- Using multiple absorption images from different runs of the experiment and averaging over many clouds. However this method requires good run-to-run experimental stability to avoid the need for normalisation of each image (as is done in [19]), since this can introduce systematic error into the measurement of variance.
- Finding and reversing the blurring of the density distribution numerically⁴. There are several methods that could be used for this purpose (see [60]), the best being a semi-blind deconvolution method, in which the blurring we calculate will be the starting point for a routine which optimises both the image and the blurring function. However, this method is computationally expensive, and it may introduce unwanted sources of noise into the data.

A combination of these methods could provide the breakthrough to allow the observation of shot-noise on Bose-condensed clouds - and therefore allow the further study of quantum correlations on these condensates.

Chapter 6 described the application of atomic shot-noise-limited absorption imaging to a precision measurement. Our cold atom interferometer is currently a factor of two away from atomic shot-noise-limited sensitivity, however as we have demonstrated atomic shot-noise-limited imaging on the same setup, our imaging technique is most likely not the cause of the instability. Once the interferometer is stabilised, it could be used to observe squeezing in our BECs [22], to make precise measurements of the fine structure constant α [28], the local gravitational field g [31], or to make precise measurements of small rotations in the setup. Another possible set of experimental realisations are the Ahronov-Bohm and Ahronov-Casher derivative experiments. These demonstrate that electromagnetic fields allow particles to be quantum mechanically scattered by topological defects when no classical force exists [61]. A particularly simple experiment of this kind which could conceivably be realised in our atom interferometer is where the arms of the atom interferometer enclose a charged wire⁵. However the execution of this experiment would not be a short-term project as it would involve re-building the vacuum chambers of the ^{87}Rb BEC machine after insertion of the required wire into the glass cell (in a vacuum sealed way) where the interferometer operates.

In the short term future, the focus should be clearly on quantitative measurements of the quantum statistics of Bose-condensed clouds. This provides direct tests of theoretical models of condensates. Improvements in measurement sensitivity using cold atom interferometry, made possible by quantum mechanical squeezing, will become detectable. This will open the door to more precise measurements of the fine structure constant (a test of quantum electrodynamics), of local gravity, of inertial effects such as rotation, and a step closer to detecting gravitational waves. Precision measurement is an old and well-crafted field with many elegant tools. Soon cold atom interferometry, using atomic shot-noise limited imaging, may become the newest addition.

⁴In computer imaging terminology, the blurring is described by a ‘point spread function’, a function like equation (3.22).

⁵Although a classical force does exist in this setup due to the polarizability of the atoms, its effect would be minimal compared with the Ahronov-Bohm scattering [62].

Statistical Distributions

A.1 Poisson Distribution

A.1.1 General Properties

The Poisson distribution is a discrete distribution in which the probability of any particular value $x \in \{0, 1, 2, 3, \dots\}$ occurring is given by

$$\Pr(X = x) = \frac{\lambda^x e^\lambda}{x!}.$$

It arises whenever a Binomial distribution with n samples and p chance of success in any sample is taken in the limit $n \rightarrow \infty$, $p \rightarrow 0$ while the mean $np = \lambda$ is held constant. It also arises when a temporal series of discrete events, which each take an exponentially distributed time t , are binned into time intervals Δt and the number n of events in each bin are counted. The Poisson distribution is approximated by a normal distribution with mean and variance λ in the limit $\lambda \rightarrow \infty$. For reference, see [63].

The mean and variance are λ :

$$\begin{aligned} E(X) &= \sum_{n=0}^{\infty} n \Pr(X = n) \\ &= \sum_{n=0}^{\infty} n \frac{\lambda^n e^\lambda}{n!} \\ &= \sum_{n=1}^{\infty} \frac{\lambda^n e^\lambda}{(n-1)!} \\ &= \lambda \sum_{n=0}^{\infty} \frac{\lambda^n e^\lambda}{n!} \\ &= \lambda \end{aligned}$$

$$\begin{aligned}
\text{Var}(X) &= \sum_{n=0}^{\infty} \Pr(X = n) (n - \text{E}(X))^2 \\
&= \lambda^2 + \sum_{n=0}^{\infty} n(n - \lambda) \frac{\lambda^n e^\lambda}{n!} \\
&= \lambda^2 + \lambda \sum_{n=1}^{\infty} (n - \lambda) \frac{\lambda^{n-1} e^\lambda}{(n-1)!} \\
&= \lambda^2 - \lambda^2 + \sum_{n=0}^{\infty} n \frac{\lambda^n e^\lambda}{n!} \\
&= \sum_{n=1}^{\infty} \frac{\lambda^n e^\lambda}{(n-1)!} \\
&= \lambda \sum_{n=0}^{\infty} \frac{\lambda^n e^\lambda}{n!} \\
&= \lambda
\end{aligned}$$

A.2 Approximations to mean and variance

For general functions $f(X)$ of a random variable X we can take a Taylor series to approximate the mean $\text{E}(f(X))$ and variance $\text{Var}(f(X))$, where $\text{E}(X) = \mu$ and $\text{Var}(X) = \sigma^2$ are known. Begin with

$$\begin{aligned}
f(X) &= f(\mu) + f'(\mu)(X - \mu) + \dots \\
&= \sum_{n=0}^{\infty} \frac{f'(\mu)}{n!} (X - \mu)^n.
\end{aligned}$$

By taking the expected value of both sides to low order we can see that

$$\text{E}(f(X)) \approx f(\mu) \quad \text{zeroth order} \tag{A.1}$$

$$\begin{aligned}
\text{E}(f(X)) &\approx f(\mu) + f'(\mu)\text{E}(X - \mu) + f''(\mu)\text{E}((X - \mu)^2) \\
&= f(\mu) + f''(\mu)\sigma^2 \quad \text{second order}
\end{aligned} \tag{A.2}$$

By constructing the variance $\text{Var}(f(X)) = \text{E}((f(X) - \text{E}(f(X)))^2)$ we see that

$$\begin{aligned}
\text{Var}(f(X)) &\approx \text{E}(f'(\mu)^2(X - \mu)^2) \\
&= f'(\mu)^2\sigma^2 \quad \text{first order}
\end{aligned} \tag{A.3}$$

$$\begin{aligned}
\text{Var}(f(X)) &\approx \text{E}\left((f'(\mu)(X - \mu) - f''(\mu)\sigma^2 + f''(\mu)(X - \mu)^2)^2\right) \\
&= \text{E}\left[\left(f'(\mu)^2(X - \mu)^2 - f''(\mu)^2\sigma^4 + f''(\mu)^2(X - \mu)^4 - 2f'(\mu)(X - \mu)f''(\mu)\sigma^2\right.\right. \\
&\quad \left.\left.- 2f''(\mu)^2\sigma^2(X - \mu)^2 + 2f'(\mu)f''(\mu)(X - \mu)^3\right)^2\right] \\
&= f'(\mu)^2\sigma^2 - 3f''(\mu)^2\sigma^4 + 2f'(\mu)f''(\mu)\text{E}((X - \mu)^3) + f''(\mu)^2\text{E}((X - \mu)^4) \\
&\quad \text{second order}
\end{aligned} \tag{A.4}$$

(A.5)

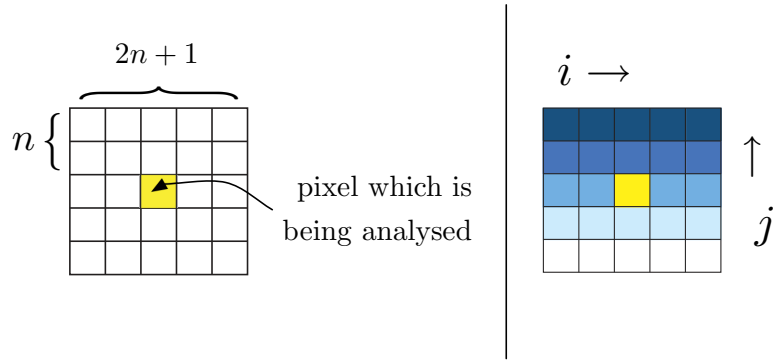


Figure A.1: **Left:** Diagram illustrating the nearby averaging procedure used to analyze absorption images. Each pixel's 'mean' is found as the average of the $(2n + 1)^2$ pixels around it. **Right:** Imagine the pixel of interest is located in the middle of a gradient. What effect will this have on the averaging? The pixels are labelled in coordinates as pixels away from the yellow one, e.g. the one in the top right corner is (n, n) and that in the bottom left is $(-n, -n)$.

where $E((X - \mu)^3)$ and $E((X - \mu)^4)$ are higher moments that we may be able to calculate depending upon the distribution of X . For example if X is a Poisson distribution with mean λ then a general formula exists¹;

$$E((X - \lambda)^n) = \left(\frac{d}{dt} \right)^n e^{\lambda(e^t - t - 1)} \Big|_{t=0}$$

so we can calculate $E((X - \lambda)^3) = \lambda$ and $E((X - \lambda)^4) = \lambda + 3\lambda^2$ and equation (A.4) becomes

$$\begin{aligned} \text{Var}(f(X)) &\approx f'(\lambda)^2 \lambda - 3f''(\lambda)^2 \lambda^2 + 2f'(\lambda)f''(\lambda)E((X - \lambda)^3) + f''(\lambda)^2 E((X - \lambda)^4) \\ &= f'(\lambda)^2 \lambda - 3f''(\lambda)^2 \lambda^2 + 2f'(\lambda)f''(\lambda)\lambda + f''(\lambda)^2 (\lambda + 3\lambda^2) \\ &= f'(\lambda)^2 \lambda + 2f'(\lambda)f''(\lambda)\lambda + f''(\lambda)^2 \lambda \\ &= [f'(\lambda) + f''(\lambda)]^2 \lambda \end{aligned}$$

while the expectation (A.2) is still

$$E(f(X)) \approx [1 + f''(\lambda)] \lambda.$$

A.3 Variance calculated by nearby averaging

One of the main methods that has been used to find a mean and deviation for each pixel, *from a single image*, was to average a square area around the pixel in question to find the 'mean' for that pixel (see the left of fig A.3). Here I calculate a simple model for how the variance as calculated relates to the actual variance of the sampled populations.

Say we take $(2n + 1)^2 = N$ samples X_i from the same distribution X . The average we

¹This can be derived using moment generating functions, $M_{X-\mu}(t) = E(e^{t(X-\mu)})$. Then each 'moment' $E((X - \mu)^n)$ may be calculated by $E((X - \mu)^n) = \frac{d^n}{dt^n} M_{X-\mu}(t)|_{t=0}$.

calculate from these samples will be denoted

$$\bar{X} = \frac{1}{N} \sum_{i=1}^N X_i.$$

The variance we calculate will be

$$\begin{aligned} E((X_i - \bar{X})^2) &= E(X_i^2 - 2X_i\bar{X} + \bar{X}^2) \\ &= E(X_i^2) - 2E(X_i\bar{X}) + E(\bar{X}^2). \end{aligned} \quad (\text{A.6})$$

Now

$$\begin{aligned} E(X_i\bar{X}) &= \frac{1}{N} \sum_{j=1}^N E(X_i X_j) \\ &= \frac{1}{N} \left[E(X^2) + \sum_{\substack{j=1 \\ i \neq j}}^N E(X_i) E(X_j) \right] \\ &= \frac{1}{N} E(X^2) + \frac{N-1}{N} E(X)^2 \\ &= \frac{1}{N} \text{Var}(X) + E(X)^2 \end{aligned}$$

Also

$$\begin{aligned} E(\bar{X}^2) &= \text{Var}(\bar{X}) + E(\bar{X})^2 \\ &= \frac{1}{N} \text{Var}(X) + E(X)^2 \end{aligned}$$

while

$$E(X_i^2) = E(X^2).$$

Putting it all together;

$$\begin{aligned} E((X_i - \bar{X})^2) &= E(X_i^2) - 2E(X_i\bar{X}) + E(\bar{X}^2) \\ &= E(X^2) + (-2+1) \left(\frac{1}{N} \text{Var}(X) + E(X)^2 \right) \\ &= \frac{N-1}{N} \text{Var}(X) \end{aligned}$$

which is in fact just the standard way to estimate the population variance $\text{Var}(X)$ from the sample variance $E((X_i - \bar{X})^2)$.

Assume now that we are on the side of a hill, i.e. each X_{ij} is a random variable with mean increasing as we go up the hill (see the right side of Figure (A.3)). Say, for example, that $E(X_{ij}) = \mu + j\nu$ where $\mu = E(X_{00})$ is the mean of the pixel of interest, and j is the vertical coordinate from the pixel of interest. Also, assume the variance also scales in this fashion, i.e. $\text{Var}(X_{ij}) = \sigma^2 + j\xi$ where $\sigma^2 = \text{Var}(X_{00})$ is the variance of the pixel of interest

The variance we calculate will be

$$\begin{aligned} \mathbb{E}((X_{00} - \bar{X})^2) &= \mathbb{E}(X_{00}^2 - 2X_{00}\bar{X} + \bar{X}^2) \\ &= \mathbb{E}(X_{00}^2) - 2\mathbb{E}(X_{00}\bar{X}) + \mathbb{E}(\bar{X}^2). \end{aligned} \quad (\text{A.7})$$

Now

$$\begin{aligned} \mathbb{E}(X_{00}\bar{X}) &= \frac{1}{N} \sum_{j=1}^N \mathbb{E}(X_{00}X_j) \\ &= \frac{1}{N} \left[\mathbb{E}(X^2) + \sum_{\substack{i,j=-n \\ i^2+j^2 \neq 0}}^n \mathbb{E}(X_{00}) \mathbb{E}(X_{ij}) \right] \\ &= \frac{1}{N} \left[\sigma^2 + \mu^2 + \sum_{\substack{i,j=-n \\ i^2+j^2 \neq 0}}^n \mu(\mu + j\nu) \right] \\ &= \frac{1}{N} [\sigma^2 + \mu^2 + (N-1)\mu^2] \\ &= \frac{\sigma^2}{N} + \mu^2 \end{aligned} \quad (\text{A.8})$$

Also

$$\begin{aligned} \mathbb{E}(\bar{X}^2) &= \text{Var}(\bar{X}) + \mathbb{E}(\bar{X})^2 \\ &= \text{Var}\left(\frac{1}{N} \sum_{i,j=-n}^n X_{ij}\right) + \mathbb{E}\left(\frac{1}{N} \sum_{i,j=-n}^n X_{ij}\right)^2 \\ &= \frac{1}{N^2} \sum_{i,j=-n}^n \text{Var}(X_{ij}) + \left[\frac{1}{N} \sum_{i,j=-n}^n \mathbb{E}(X_{ij}) \right]^2 \\ &= \frac{1}{N^2} \sum_{i,j=-n}^n (\sigma^2 + j\xi) + \left[\frac{1}{N} \sum_{i,j=-n}^n \mu + j\nu \right]^2 \\ &= \frac{\sigma^2}{N} + \mu^2 \end{aligned} \quad (\text{A.9})$$

while

$$\begin{aligned} \mathbb{E}(X_{00}^2) &= \text{Var}(X_{00}) + \mathbb{E}(X_{00})^2 \\ &= \sigma^2 + \mu^2 \end{aligned}$$

Putting it all together;

$$\begin{aligned} \mathbb{E}((X_{00} - \bar{X})^2) &= \mathbb{E}(X_{00}^2) - 2\mathbb{E}(X_{00}\bar{X}) + \mathbb{E}(\bar{X}^2) \\ &= \sigma^2 + \mu^2 + (-2+1)\left(\frac{\sigma^2}{N} + \mu^2\right) \\ &= \frac{N-1}{N}\sigma^2 \end{aligned}$$

which is the same result we got before. This is because the sums on lines (A.8) and (A.9) reduced to their trivial values by cancellation of the changes either side of the pixel of interest. This will not occur if the distributions either side of the pixel of interest are asymmetrical, for instance at the top of a hill, or over a region where a slope flattens out.

Bibliography

- [1] R. M. Godun. Prospects for atom interferometry. *Contemporary Physics*, 42(2):77, 95 2001.
- [2] M. H. Anderson, J. R. Ensher, M. R. Matthews, C. E. Wieman, and E. A. Cornell. Observation of Bose-Einstein Condensation in a Dilute Atomic Vapor. *Science*, 269(5221):198–201, 7 1995. Available from: <http://www.sciencemag.org/cgi/content/abstract/269/5221/198>.
- [3] E. A. Cornell and C. E. Wieman. Nobel Lecture: Bose-Einstein condensation in a dilute gas, the first 70 years and some recent experiments. *Reviews of Modern Physics*, 74(3), 08 2002. Available from: <http://link.aps.org/abstract/RMP/v74/p875>.
- [4] J. R. Ensher, D. S. Jin, M. R. Matthews, C. E. Wieman, and E. A. Cornell. Bose-Einstein condensation in a Dilute Gas: Measurement of Energy and Ground-State Occupation. *Physical Review Letters*, 77(25):4984, 1996.
- [5] J. R. Ensher. *The first experiments with Bose-Einstein Condensation of Rubidium 87*. PhD thesis, University of Colorado, 1998.
- [6] Ehud Altman, Eugene Demler, and Mikhail D. Lukin. Probing many-body states of ultracold atoms via noise correlations. *Phys. Rev. A*, 70(1):013603, Jul 2004. doi: 10.1103/PhysRevA.70.013603.
- [7] Simon Fölling, Fabrice Gerbier, Artur Widera, Olaf Mandel, Tatjana Gericke, and Immanuel Bloch. Spatial quantum noise interferometry in expanding ultracold atom clouds. *Nature*, 434:481, March 2005.
- [8] M. Greiner, C. A. Regal, J. T. Stewart, and D. S. Jin. Probing Pair-Correlated Fermionic Atoms through Correlations in Atom Shot Noise. *Phys. Rev. Lett.*, 94(11):110401, Mar 2005. doi:10.1103/PhysRevLett.94.110401.
- [9] T. Jeltes, J. M. McNamara, W. Hogervorst, W. Vassen, V. Krachmalnicoff, M. Schellekens, A. Perrin, H. Chang, D. Boiron, A. Aspect, and C. I. Westbrook. Comparison of the hanbury brown-twiss effect for bosons and fermions. *Nature*, 445(7126):402–405, January 2007. Available from: <http://dx.doi.org/10.1038/nature05513>.
- [10] C. Bruder, R. Fazio, and G. Schön. The Bose-Hubbard model: from Josephson junction arrays to optical lattices. *Annalen der Physik*, 14(9):566–577, August 2005.
- [11] Fabrice Gerbier, Artur Widera, Simon Fölling, Olaf Mandel, Tatjana Gericke, and Immanuel Bloch. Interference pattern and visibility of a Mott insulator. *Phys. Rev. A*, 72(5):053606, Nov 2005. doi:10.1103/PhysRevA.72.053606.
- [12] R. de Picciotto, M. Reznikov, M. Heiblum, V. Umansky, G. Bunin, and D. Mahalu. Direct Observation of a Fractional Charge. *Nature*, 389:162, September 1997.

- [13] L. Saminadayar, D. C. Glattli, Y. Jin, and B. Etienne. Observation of the $e/3$ Fractionally Charged Laughlin Quasiparticle. *Phys. Rev. Lett.*, 79(13):2526–2529, Sep 1997. doi:10.1103/PhysRevLett.79.2526.
- [14] M. Hafezi, A. S. Sorensen, E. Demler, and M. D. Lukin. Fractional quantum Hall effect in optical lattices. *Physical Review A (Atomic, Molecular, and Optical Physics)*, 76(2):023613, 2007. Available from: <http://link.aps.org/abstract/PRA/v76/e023613>, doi:10.1103/PhysRevA.76.023613.
- [15] A. Montina and F. T. Arecchi. Atomic density fluctuations in Bose-Einstein condensates. *Phys. Rev. A*, 68(5):053608, Nov 2003. doi:10.1103/PhysRevA.68.053608.
- [16] Siegfried Grossmann and Martin Holthaus. Fluctuations of the Particle Number in a Trapped Bose-Einstein Condensate. *Phys. Rev. Lett.*, 79(19):3557–3560, Nov 1997. doi:10.1103/PhysRevLett.79.3557.
- [17] Zbigniew Idziaszek, Mariusz Gajda, Patrick Navez, Martin Wilkens, and Kazimierz Rzaz'ewski. Fluctuations of the Weakly Interacting Bose-Einstein Condensate. *Phys. Rev. Lett.*, 82(22):4376–4379, May 1999. doi:10.1103/PhysRevLett.82.4376.
- [18] Christoph Weiss and Martin Wilkens. Particle number counting statistics in ideal Bose gases. *Opt. Express*, 1(10):272–283, 1997. Available from: <http://www.opticsexpress.org/abstract.cfm?URI=oe-1-10-272>.
- [19] J. Esteve, J.-B. Trebbia, T. Schumm, A. Aspect, C. I. Westbrook, and I. Bouchoule. Observations of Density Fluctuations in an Elongated Bose Gas: Ideal Gas and Quasicondensate Regimes. *Physical Review Letters*, 96(13):130403–+, April 2006. arXiv:arXiv:cond-mat/0510397, doi:10.1103/PhysRevLett.96.130403.
- [20] C.-S. Chuu, F. Schreck, T.P. Meyrath, J. L. Hanssen, G. N. Price, and M. G. Raizen. Direct Observation of Sub-Poissonian Number Statistics in a Degenerate Bose Gas. *Physical Review Letters*, 95(260403), December 2005.
- [21] Vittorio Giovannetti, Seth Lloyd, and Lorenzo Maccone. Quantum-Enhanced Measurements: Beating the Standard Quantum Limit. *Science*, 306(5700):1330–1336, 11 2004. Available from: <http://www.sciencemag.org/cgi/content/abstract/306/5700/1330>.
- [22] Mattias T. Johnsson and Simon A. Haine. Generating Quadrature Squeezing in an Atom Laser through Self-Interaction. *Physical Review Letters*, 99(1):010401, 2007. Available from: <http://link.aps.org/abstract/PRL/v99/e010401>, doi:10.1103/PhysRevLett.99.010401.
- [23] S. A. Haine and J. J. Hope. Outcoupling from a bose-einstein condensate with squeezed light to produce entangled-atom laser beams. *Phys. Rev. A*, 72(3):033601, Sep 2005. doi:10.1103/PhysRevA.72.033601.
- [24] J. Esteve, C. Gross, A. Weller, S. Giovanazzi, and M. K. Oberthaler. Squeezing and entanglement in a Bose-Einstein condensate. *Nature*, 455(7217):1216–1219, 10 2008. Available from: <http://dx.doi.org/10.1038/nature07332>.

- [25] David W. Keith, Christopher R. Ekstrom, Quentin A. Turchette, and David E. Pritchard. An interferometer for atoms. *Physical Review Letters*, 66(21), 05 1991. Available from: <http://link.aps.org/abstract/PRL/v66/p2693>.
- [26] O. Carnal and J. Mlynek. Young's double-slit experiment with atoms: A simple atom interferometer. *Physical Review Letters*, 66(21), 05 1991. Available from: <http://link.aps.org/abstract/PRL/v66/p2689>.
- [27] A Miffre, M Jacquay, M Buchner, G Trenec, and J Vigue. Atom interferometry. *Physica Scripta*, 74(2):C15–C23, 2006. Available from: <http://stacks.iop.org/1402-4896/74/C15>.
- [28] Andreas Wicht, Joel M Hensley, Edina Sarajlic, and Steven Chu. A Preliminary Measurement of the Fine Structure Constant Based on Atom Interferometry. *Physica Scripta*, T102:82–88, 2002. Available from: <http://stacks.iop.org/1402-4896/T102/82>.
- [29] Pierre Clade, Estefania de Mirandes, Malo Cadoret, Saida Guellati-Khelifa, Catherine Schwob, Francois Nez, Lucile Julien, and Francois Biraben. Determination of the Fine Structure Constant Based on Bloch Oscillations of Ultracold Atoms in a Vertical Optical Lattice. *Physical Review Letters*, 96(3):033001, 2006. Available from: <http://link.aps.org/abstract/PRL/v96/e033001>, doi:10.1103/PhysRevLett.96.033001.
- [30] H. Müller, S. W. Chiow, Q. Long, C. Vo, and S. Chu. A new photon recoil experiment: towards a determination of the fine structure constant. *Applied Physics B: Lasers and Optics*, 84(4):633–642, 09 2006. Available from: <http://dx.doi.org/10.1007/s00340-006-2279-x>.
- [31] J. M. McGuirk, G. T. Foster, J. B. Fixler, M. J. Snadden, and M. A. Kasevich. Sensitive absolute-gravity gradiometry using atom interferometry. *Phys. Rev. A*, 65(3):033608, Feb 2002. doi:10.1103/PhysRevA.65.033608.
- [32] Savas Dimopoulos, Peter W. Graham, Jason M. Hogan, Mark A. Kasevich, and Surjeet Rajendran. Atomic gravitational wave interferometric sensor. *Physical Review D (Particles, Fields, Gravitation, and Cosmology)*, 78(12):122002, 2008. Available from: <http://link.aps.org/abstract/PRD/v78/e122002>, doi:10.1103/PhysRevD.78.122002.
- [33] Mi-lasers 780nm diode [online]. Available from: <http://www.mi-lasers.com/cgi-bin/shopper.cgi?preadd=action&key=LT021MDO> [cited 28/10/09].
- [34] P. A. Altin. Sympathetic Cooling of Rubidium 85. Honours Thesis, 2007.
- [35] Daniel Günther Greif. Evaporative Cooling and Bose-Einstein Condensation. Master's thesis, Stony Brook University, 2007.
- [36] David R. Lide, editor. *CRC Handbook of Chemistry and Physics*. Taylor and Francis Group LLC, 89th edition, 2009.
- [37] C. J. Foot. *Atomic Physics*. Oxford University Press, 2005.

- [38] D. A. Steck. Rubidium 87 D Line Data. Available from: <http://steck.us/alkalidata>.
- [39] Franco Dalfovo, Stefano Giorgini, Lev P. Pitaevskii, and Sandro Stringari. Theory of Bose-Einstein condensation in trapped gases. *Reviews of Modern Physics*, 71(3), 04 1999. Available from: <http://link.aps.org/abstract/RMP/v71/p463>.
- [40] W. Ketterle, D.S. Durfee, and D.M. Stamper-Kurn. Making, Probing and Understanding Bosé-Einstein Condensates. 1999.
- [41] L. D. Landau, E. M. Lifshitz, and L. P. Pitaevskii. *Statistical Physics (Part 1)*. Pergamon Press., 3rd edition, 1980.
- [42] W. Belzig, C. Schroll, and C. Bruder. Density correlations in ultracold atomic Fermi gases. *Physical Review A (Atomic, Molecular, and Optical Physics)*, 75(6):063611, 2007. Available from: <http://link.aps.org/abstract/PRA/v75/e063611>, doi:10.1103/PhysRevA.75.063611.
- [43] Wolfgang Ketterle and Hans-Joachim Miesner. Coherence properties of Bose-Einstein condensates and atom lasers. *Physical Review A*, 56(4), 10 1997. Available from: <http://link.aps.org/abstract/PRA/v56/p3291>.
- [44] Michael Robin Matthews. *Two-Component Bose-Einstein Condensation*. PhD thesis, University of Colorado, 1999.
- [45] Point Grey Research. Grasshopper Technical Reference Manual, 2008. Available from: <http://www.ptgrey.com/products/grasshopper/index.asp>.
- [46] Yaxia Liu, Hai ming Bao, Jie Li, Jin Ruan, and Zhihang Hao. Measuring the system gain of the TDI CCD remote sensing camera. volume 5633, pages 520–526. SPIE, 2005. Available from: <http://link.aip.org/link/?PSI/5633/520/1>, doi:10.1117/12.576184.
- [47] Anthony Mark Fox. *Quantum optics: an introduction*. Oxford University Press, 2006. Available from: http://books.google.com.au/books?id=2_ZP-LDF9jkC&lpg=PA85&ots=MeVxLOVI_C&dq=thermal%20light%20poisson&pg=PA85#v=onepage&q=thermal%20light%20poisson&f=false.
- [48] L. Mandel and E. Wolf. *Optical Coherence and Quantum Optics*. Cambridge University Press, 1995.
- [49] Photometrics. CoolSnap HQ Monochrome Datasheet, October 2009. Available from: <http://taltos.stanford.edu/docs/cshq.pdf>.
- [50] C.J. Pethick and H. Smith. *Bose-Einstein condensation in dilute gases*. Cambridge University Press, 2002.
- [51] D. Griffiths. *Introduction to Quantum Mechanics*. Pearson Prentice Hall, 2005.
- [52] W. Ketterle and N. J. van Druten. Bose-einstein condensation of a finite number of particles trapped in one or three dimensions. *Physical Review A*, 54(1):656–660, July 1996.

-
- [53] J. Szczepkowski, R. Gartman, M. Witkowski, L. Tracewski, M. Zawada, and W. Gawlik. Analysis and calibration of absorptive images of Bose-Einstein condensate at nonzero temperatures. *Review of Scientific Instruments*, 80(5):053103–+, May 2009. [arXiv:0811.4034](https://arxiv.org/abs/0811.4034), doi:10.1063/1.3125051.
 - [54] G. B. Jo, Y. Shin, S. Will, T. A. Pasquini, M. Saba, W. Ketterle, D. E. Pritchard, M. Vengalattore, and M. Prentiss. Long Phase Coherence Time and Number Squeezing of Two Bose-Einstein Condensates on an Atom Chip. *Physical Review Letters*, 98(3):030407–4, 01 2007. Available from: <http://link.aps.org/abstract/PRL/v98/e030407>.
 - [55] D. Döring, J. E. Debs, N. P. Robins, C. Figl, P. A. Altin, and J. D. Close. Ramsey interferometry with an atom laser. *arXiv:0812.2310 (Preprint, Accepted to Optics Express)*.
 - [56] Holger Müller, Sheng wey Chiow, Quan Long, Sven Herrmann, and Steven Chu. Atom Interferometry with up to 24-Photon-Momentum-Transfer Beam Splitters. *Physical Review Letters*, 100(18):180405, 2008. Available from: <http://link.aps.org/abstract/PRL/v100/e180405>, doi:10.1103/PhysRevLett.100.180405.
 - [57] Mark Kasevich and Steven Chu. Atomic interferometry using stimulated Raman transitions. *Phys. Rev. Lett.*, 67(2):181–184, Jul 1991. doi:10.1103/PhysRevLett.67.181.
 - [58] Thorlabs: Near IR Achromatic Doublets [online]. Available from: http://www.thorlabs.com/NewGroupPage9.cfm?ObjectGroup_ID=4066.
 - [59] C. G. Townsend, N. H. Edwards, K. P. Zetie, C. J. Cooper, J. Rink, and C. J. Foot. High-density trapping of cesium atoms in a dark magneto-optical trap. *Phys. Rev. A*, 53(3):1702–1714, Mar 1996. doi:10.1103/PhysRevA.53.1702.
 - [60] BiAlith Research Results [online]. Available from: <http://www.bialith.com/BAResearch.htm>.
 - [61] Martin Wilkens. Quantum phase of a moving dipole. *Phys. Rev. Lett.*, 72(1):5–8, Jan 1994. doi:10.1103/PhysRevLett.72.5.
 - [62] U. Leonhardt and M. Wilkens. Aharonov-Bohm scattering of neutral atoms. *EPL (Europhysics Letters)*, 42(4):365–370, 1998. Available from: <http://stacks.iop.org/0295-5075/42/365>.
 - [63] Dennis Wackerly, Richard L. Scheaffer, and William Mendenhall. *Mathematical Statistics With Applications*. Duxbury Pr, 6th edition, May 2001.